Title

Amplitude dynamics of the charge density wave in LaTe3 : Theoretical description of pump-probe experiments

Journal

Physical Review B, 101(5)

ISSN

2469-9950

Authors

Dolgirev, Pavel E
Rozhkov, AV
Zong, Alfred
et al.

Publication Date

2020-02-01

DOI

10.1103/physrevb.101.054203

Peer reviewed

Amplitude dynamics of charge density wave in $LaTe_3$: theoretical description of pump-probe experiments

Pavel E. Dolgirev,[1,*] A.V. Rozhkov,[1,2,†] Alfred Zong,[3] Anshul Kogar,[3] Nuh Gedik,[3] and Boris V. Fine[1,4,‡]

[1] *Skolkovo Institute of Science and Technology, Skolkovo Innovation Center, 3 Nobel St., Moscow 143026, Russia*
[2] *Institute for Theoretical and Applied Electrodynamics, Russian Academy of Sciences, Moscow, 125412, Russia*
[3] *Massachusetts Institute of Technology, Department of Physics, Cambridge, Massachusetts 02139, USA*
[4] *Institute for Theoretical Physics, University of Heidelberg, Philosophenweg 12, 69120 Heidelberg, Germany*

(Dated: April 23, 2019)

We formulate a dynamical model to describe a photo-induced charge density wave (CDW) quench transition and apply it to recent multi-probe experiments on $LaTe_3$ [A. Zong *et al.*, Nat. Phys. (2019)]. Our approach relies on coupled time-dependent Ginzburg-Landau equations tracking two order parameters that represent the modulations of the electronic density and the ionic positions. We aim at describing the amplitude of the order parameters under the assumption that they are homogeneous in space. This description is supplemented by a three-temperature model, which treats separately the electronic temperature, the temperature of the lattice subsystem coupled to the CDW order, and the temperature of the rest of the lattice. The broad scope of available data for $LaTe_3$ and similar materials as well as the synergy between different time-resolved spectroscopies allow us to extract model parameters. The resulting calculations are in good agreement with previous ultra-fast electron diffraction experiments, reproducing qualitative and quantitative features of the CDW amplitude evolution during the initial few picoseconds after photoexcitation.

I. INTRODUCTION

Dynamics of phase transitions associated with spontaneous symmetry breaking remains an interesting subject both theoretically and experimentally. Thanks to the advances in time-resolved pump-probe techniques, it is now possible[1–8] to perturb an ordered state and then monitor its fast non-adiabatic recovery. For strong perturbations, one can observe a passage through an ordering transition, register the emergence of ordered phases, and measure time evolution of diverse system parameters with a subpicosecond resolution. The responses of ordered phases, such as superconducting phase[1,6], spin-density-wave[2,7,9] and charge-density-wave[3–5,8,10–24] phases, have been studied this way.

The focus of the present work is on the non-equilibrium dynamics across a CDW transition. Despite long and thorough scrutiny[25,26], the CDW state continues to generate ample amount of research activity motivated by interesting many-body physics (collective transport phenomena[26–29], non-mean field critical exponents[30–32], exotic metastable 'hidden' states[33–36]), and large number of experimentally available model systems. In particular, one can mention such 'classical' CDW materials as[37–40] $NbSe_3$, $NbSe_2$, TaS_2, blue bronzes $K_{0.30}MoO_3$ and $Rb_{0.30}MoO_3$. The CDW compound $LaTe_3$ investigated in the present work belongs to the family of rare-earth tritellurides. CDW phase was also observed and actively investigated in other members of this family[3–5,22,31,41–50].

Recently, we reported[8] results of an experimental multi-probe study of a photo-induced CDW transition in $LaTe_3$. In these experiments, the post-pump relaxation was monitored with the help of three different time-resolved techniques: ultra-fast electron diffraction (UED), transient reflectivity, and time- and angle-resolved photo-emission spectroscopy (tr-ARPES). These measurements delivered a wealth of complementary information about both electronic and lattice degrees of freedom. In particular, they produced evidence that the phase relaxation of the CDW order is significantly slower than that of the CDW amplitude. The present work is dedicated to developing theoretical description of the dynamics of the CDW amplitude only. The phase relaxation is to be investigated elsewhere.

Among theoretical tools[25,51–57] capturing the dynamics of an order parameter, the time-dependent Ginzburg-Landau (TDGL) equation[3,4,21,22,58–62] is one of the most popular. Despite the known issues with its microscopic justification[63], TDGL formalism remains in wide use due to its simplicity and intuitive appeal. The TDGL approach will be one of the building blocks for our modeling.

A CDW state, by its very nature, depends crucially on electrons and lattice cooperation. As a result, a generic non-equilibrium evolution of a CDW system involves both electronic and lattice degrees of freedom coupled together into a complex kinetic ensemble. In the experiment of Ref. 8, a laser pumping pulse excites mostly electronic degrees of freedom, while keeping the lattice initially unaffected. The ensuing internal equilibration of the electronic subsystem is much faster than that of the lattice. Consequently, the theoretical TDGL modeling should treat the CDW lattice distortions and the electronic density modulations as two separate dynamical variables[59,60]. Furthermore, the physical processes in a photo-excited system at the early relaxation stages cannot be characterized by a single temperature even crudely. Therefore, we supplement the TDGL equations by the so-called three-temperature model[64–66], which as-

signs separate temperatures to (i) electrons, (ii) phonons whose wave vector is close to the CDW ordering vector, and (iii) all other phonons. Despite large number of parameters in our formalism, the broad scope of the data from Ref. 8, together with numerous experimental results for other rare-earth tritellurides, allows us to devise sensible parameter assignment protocols.

Resulting numerical simulations reproduce the experiment[8] both qualitatively and quantitatively. Specifically, we capture the measured evolution of the CDW peak intensity. Our model also reproduces non-monotonic dynamics for the intensity of the UED Bragg peak of the underlying crystal lattice[8].

The paper is organized as follows. In Sec. II we present the main formalism. Next, in Sec. III, the parameter values for the dynamical equations are fixed. Numerical simulations are compared with experimental data in Sec. IV. Sec. V contains discussion and conclusions. Technically involved derivations are relegated to the Appendices.

II. THEORETICAL FORMALISM

In this section we introduce our theoretical model of non-equilibrium CDW evolution. The model formalism consists of two pieces: the TDGL equations and the three-temperature model.

A. TDGL sector

1. *Static Landau functional*

The CDW state is characterized by both the modulation of the electronic density

$$\delta\rho_{\rm e}(\mathbf{r}) = A\exp(i\mathbf{Q}\cdot\mathbf{r}) + \text{c.c.}, \tag{1}$$

and the displacements of ions

$$\delta\mathbf{r}_n = [iu\exp(i\mathbf{Q}\cdot\mathbf{r}_n) + \text{c.c.}]\,\hat{e}_{\rm CDW} \tag{2}$$

from high-symmetry lattice positions $\mathbf{r}_n$. Here $\mathbf{Q}$ is the CDW wave vector; $\hat{e}_{\rm CDW}$ is the unit vector along the CDW displacements. Quantities A and u describe complex electronic and lattice order parameters. In Appendix A, we discuss a way to experimentally determine the lattice order parameter based on diffraction measurements.

To describe equilibrium properties of the CDW system, one can introduce a Landau-type functional, which depends either exclusively on A, or exclusively on u. However, to account for the dynamical properties of the CDW during photo-induced transition, we need to retain both A and u. We then write[59,60]:

$$\mathcal{F}[A,u] = -a|A|^2 + \frac{b}{2}|A|^4 - \eta(Au^* + A^*u) + \mathcal{K}|u|^2, \tag{3}$$

where a, b, η and $\mathcal{K}$ are the expansion parameters. The first two terms in Eq. (3) represent purely electronic subsystem. The last term corresponds to the elastic lattice energy, which increases if the ions are shifted from their most symmetrical positions. Finally, the term proportional to η describes the electron-lattice coupling – often the main driving force behind the CDW transition.

Below we assume that parameters of the Landau functional are temperature independent, except for

$$a = \alpha(T_0 - T), \tag{4}$$

where α is a positive proportionality coefficient, T is the system temperature, and T_0 is the "bare" transition temperature for a hypothetical situation of vanishing electron-lattice interaction. (In principle, however, T_0 can be negative.) Due to finite coupling between A and u, the actual transition into the ordered phase occurs at the critical temperature

$$T_c = T_0 + \frac{\eta^2}{\alpha\mathcal{K}}. \tag{5}$$

For $LaTe_3$, we approximate[8] $T_c \approx 670$K. As for T_0, it can be estimated with the help of the relation

$$T_0 = T_c(1-\zeta), \tag{6}$$

where

$$\zeta = \frac{\eta^2}{\alpha T_c\mathcal{K}}. \tag{7}$$

This parameter characterizes electron-phonon interaction strength. For the parameters chosen in Sec. III to represent $LaTe_3$, we obtained $T_0 = -67\,$K. The negative sign of T_0 does not create any theoretical difficulty, since "bare" T_0 does not enter the formalism — only T_c does.

Minimizing the functional at $T < T_c$, one finds equilibrium values of the order parameters:

$$A_{\rm eq} = \sqrt{\frac{\alpha}{b}(T_c - T)}, \quad u_{\rm eq} = \frac{\eta}{\mathcal{K}}A_{\rm eq}. \tag{8}$$

For our calculations, it is convenient to work with the dimensionless quantities:

$$x = \frac{A}{A_{\rm eq}(T=0)}, \quad y = \frac{u}{u_{\rm eq}(T=0)}. \tag{9}$$

For $T \le T_c$, equilibrium values of x and y are

$$x_{\rm eq} = y_{\rm eq} = \sqrt{\Theta}, \tag{10}$$

where $\Theta = (T_c - T)/T_c$ is the reduced temperature.

2. *Time-dependent equations*

The next step is to generalize the static Landau theory to non-equilibrium situations. We will describe the dynamics of the electronic degree of freedom A as

$$\Gamma\frac{dA}{dt} = -\frac{\partial\mathcal{F}}{\partial A^*} = aA - b|A|^2A + \eta u, \tag{11}$$

where Γ is a damping parameter. In dimensionless variables, Eq. (11) reads

$$\tau_0 \frac{dx}{dt} - \Theta x + |x|^2 x + \zeta(x-y) = 0, \quad \tau_0 = \frac{\Gamma}{\alpha T_c}. \quad (12)$$

Here τ_0 is the electronic relaxation time.

From the viewpoint of the true microscopic kinetics, the fact that the time evolution of parameter x is controlled by the first term in Eq. (12) is a crude oversimplification. However, for the purposes of the present work, such an oversimplification should be sufficient given that we are mainly interested in a much longer timescale of variable y, which is, in turn, determined by the fact that ions are much heavier and thus much slower than electrons. It is only important for us that variable x adjusts itself to the instantaneous value of variable y on the fast timescale of τ_0 set by electron-electron interaction. Whether or not this adjustment is actually controlled by Eq. (12) is less important. Since we are not interested in sub-picosecond details, we define "instantaneous equilibrium" value $\bar{x}$ as a root of the equation

$$\Theta \bar{x} - \bar{x}^3 + \zeta(y - \bar{x}) = 0, \quad (13)$$

and approximate the dynamics of x as a relaxation to $\bar{x}$ with some characteristic scale τ_0. This is precisely what Eq. (12) aims to capture.

To model the evolution of u we should keep in mind that u is associated with displacements of heavy ions, which can be viewed approximately as classical objects. The forces acting on the ions are

$$f_u = -\frac{d\mathcal{F}}{du^*} = -\mathcal{K}u + \eta A. \quad (14)$$

The term proportional to $\mathcal{K}$ in Eq. (14) describes elastic force that pulls ions back to their high-symmetry positions. The term proportional to η originates from the interaction with the modulated electron density (1). By adding damping, we arrive at classical equation of motion for u. In the rescaled variables, it reads

$$\frac{1}{\omega_0^2}\frac{d^2y}{dt^2} + \frac{\gamma_y}{\omega_0}\frac{dy}{dt} + (y - x) = 0, \quad (15)$$

where $\omega_0 = \sqrt{\mathcal{K}/m}$ is unrenormalized phonon frequency; m is the ion mass parameter; γ_y describes damping. Equations (12) and (15) constitute the desired TDGL equations in dimensionless form.

B. Three-temperature model

Temperature T that appears in Eq. (4) is the electronic temperature which we now denote as T_e. The TDGL equation (12) thus depends on T_e. Therefore, we need to describe the time evolution of the electronic temperature. Our model is based on the following reasoning. During laser-induced photo-excitation, all photons are mostly absorbed by the electronic subsystem. As a result, right after this laser pulse, electronic subsystem is far from equilibrium. However, on the time scale τ_0, electronic subsystem approaches quasistationary thermal state with initial temperature $T_\mathrm{e}(0) \sim 1000\,\mathrm{K}$, which significantly exceeds the initial lattice temperature $T_\mathrm{L}(0) \sim 300\,\mathrm{K}$. Lattice phonons, whose heat capacity is much larger than that of the electrons, act as a bath which slowly absorbs energy of the hot electrons. Let us emphasize that during this process it can happen that phonon distribution function becomes highly non-thermal.

Probably the simplest approach to capture the above dynamics is to introduce two-temperature model[67–69] describing evolution of T_e and T_L. However, given all available experimental data – including (i) heat capacity measurements in $LaTe_3$, (ii) UED data (in particular, Bragg peaks long-time dynamics), (iii) short-time transient-reflectivity dynamics, and (iv) tr-ARPES data, which allows to estimate electronic heat capacity (see Sec. III below) – we were unable to adequately reproduce all the experiments using two-temperature model. Specifically, the interpretation of the experiments requires the initial fast relaxation of T_e followed by a noticeably slower relaxation (cf. Fig. 2), whereas the natural behavior of the two-temperature model is controlled by a single time scale describing the energy exchange between the electronic and the lattice subsystems.

To overcome this problem, we choose to consider a three-temperature model, which is introduced below. This model implies that phonon distribution function is now described by two temperatures $T_{\mathrm{L}1}$ and $T_{\mathrm{L}2}$. The motivation behind such a theoretical construction is as follows. We expect that, during the cooling process, electrons transfer their energy preferentially to phonons with wave vectors $\mathbf{k}$ in the part of the Brillouin zone around the CDW ordering vector $\mathbf{Q}$. We, therefore, split the lattice phonons into two subgroups: (i) "CDW phonons" — all those contained in the above-mentioned BZ region around the CDW ordering vector, and (ii) "non-CDW phonons", i.e. the rest of the phonons. The CDW phonons are to be characterized by temperature $T_{\mathrm{L}2}$, while non-CDW phonons by temperature $T_{\mathrm{L}1}$. Following the preceding argument, we neglect the direct energy transfer between the electronic subsystem and the non-CDW phonons. The post-pulse temperature dynamics is then described by the three-temperature model[64,65]:

$$C_\mathrm{e}(T_\mathrm{e})\frac{dT_\mathrm{e}}{dt} = -G_{\mathrm{eL}}(T_\mathrm{e} - T_{\mathrm{L}2}), \quad (16)$$

$$C_{\mathrm{L}1}\frac{dT_{\mathrm{L}1}}{dt} = -G_{\mathrm{LL}}(T_{\mathrm{L}1} - T_{\mathrm{L}2}), \quad (17)$$

$$C_{\mathrm{L}2}\frac{dT_{\mathrm{L}2}}{dt} = -G_{\mathrm{eL}}(T_{\mathrm{L}2} - T_\mathrm{e}) - G_{\mathrm{LL}}(T_{\mathrm{L}2} - T_{\mathrm{L}1}). \quad (18)$$

Here $C_{\mathrm{L}1}$ and $C_{\mathrm{L}2}$ are heat capacities of the non-CDW phonons and of the CDW phonons, respectively; G_{eL} and G_{LL} describe energy exchange rates. Electronic heat capacity is a temperature-dependent quantity $C_\mathrm{e}(T_\mathrm{e})$, whose functional form is discussed in subsection III B.

Initial conditions for Eqs. (16-18) are the following. For

TDGL sector		Temperature-evolution sector	
Parameter	Value	Parameter	Value
$\omega_0/(2\pi)$	3.1 THz	c_0	1.1 mJ/mol·K^2
τ_0	20 fs	c	4 mJ/mol·K^2
ζ	1.1	$C_{\rm tot}$	99.7 J/mol·K
γ_y	0.04	κ	0.2
T_c	670 K	$G_{\rm eL}$	5.5 J/ps·K·mol
		$\tau_{\rm DW}$	2.2 ps

TABLE I. Parameters used for numerical simulations of Eqs. (12) and (15), and Eqs. (16–18).

the lattice, $T_{\rm L1}(0) = T_{\rm L2}(0) = T_{\rm env}$, where $T_{\rm env} = 300\,{\rm K}$ is the environment temperature. For electrons, $T_{\rm e}(0)$ is defined as the temperature right after the laser pulse and the ensuing fast electronic self-thermalization. The value $T_{\rm e}(0)$ is, therefore, a function of absorbed electromagnetic energy per mole, which is, in turn, proportional to (i) the photoexcitation density F (the number of absorbed photons per unit volume), (ii) the pump photon energy $\hbar\omega_\gamma = 1.19\,{\rm eV} = 1.9\cdot 10^{-19}\,{\rm J}$, and (iii) the molar volume $\mathcal{V} = 76.8\,{\rm cm}^3/{\rm mol}$ of $LaTe_3$. The equation determining $T_{\rm e}(0)$ is the energy balance condition

$$\hbar\omega_\gamma \mathcal{V} F = \int_{T_{\rm env}}^{T_{\rm e}(0)} C_{\rm e}(T) dT. \tag{19}$$

III. CHOICE OF PARAMETERS

Our formalism in its final version consists of five equations: Eqs. (12) and (15) constitute the TDGL sector, while Eqs. (16–18) is the temperature-evolution sector. To perform simulations, we need to select specific values for the model parameters: ω_0, τ_0, ζ, and γ_y in the TDGL sector; and $C_{\rm L1}$, $C_{\rm L2}$, $G_{\rm eL}$, and $G_{\rm LL}$ in the temperature-evolution sector. We also need a concrete functional form of the temperature dependence of the electronic heat capacity $C_{\rm e}(T_{\rm e})$.

Since the total number of free parameters is large, extracting their values through an indiscriminate fitting might produce misleading results. To circumvent this issue, we split the whole task of estimating the model parameters into several steps: in each step only a small number of the unknowns is fixed. This approach relies on the availability of a broad array of experimental results for the rare-earth tritellurides, in particular $LaTe_3$. Namely, the information about temperature dependence of phonon spectrum in RTe_3 will be used to fix the TDGL parameters; the synergy between tr-ARPES, UED, and transient reflectivity data[8] for $LaTe_3$ will guide us to obtain the remaining three-temperature model parameters.

For convenience, in Table I, we collect the final values.

A. TDGL parameters

Phonon spectrum in RTe_3 and its temperature dependence were investigated in many experiments[8,45,47,70,71]. At the same time, one can apply small-oscillations formalism[59,60] to the TDGL equations (12) and (15) in order to obtain theoretically the properties of the CDW amplitude mode (AM). Matching the theoretical results with the spectral data, we fix the TDGL parameters, at least partially.

Equations (12) and (15) in the regime of small oscillations are investigated in Appendix B. Equations (B6) and (B7) for the resulting eigenvalue problem implicitly define functional dependencies $\omega_{\rm AM}(\omega_0,\tau_0,\zeta,\gamma_y)$ and $\gamma_{\rm AM}(\omega_0,\tau_0,\zeta,\gamma_y)$. At $T = 300\,{\rm K}$, we know from the peak position and the peak width of the Fourier transform of the measured transient reflectivity oscillations[8] that

$$\frac{\omega_{\rm AM}}{2\pi} = \nu_{\rm AM} = 2.2\,{\rm THz},\ \ \gamma_{\rm AM} = 1.26\cdot 10^{12}\,{\rm s}^{-1}. \tag{20}$$

We use the above values together with Eq. (B6) to impose two constraints on parameters ω_0, τ_0, ζ, and γ_y, see derivation of Eqs. (B10) and (B11). Thereby, we reduce the total number of adjustable TDGL parameters from four to two. For our analysis, it is convenient to treat Eqs. (B10) and (B11) as definitions of the implicit functions $\gamma_y(\omega_0,\tau_0)$ and $\zeta(\omega_0,\tau_0)$, which specify the dependence of ζ and γ_y on ω_0 and τ_0. Thus, once ω_0 and τ_0 are found, the TDGL sector contains no unknown parameters.

Evaluating ω_0 and τ_0, one must be mindful of several relevant theoretical and experimental restrictions. The first of them is the physical requirement $\gamma_y(\omega_0,\tau_0) \geq 0$. It limits the allowed space for ω_0 and τ_0 to the region left and below the red curve in Fig. 1.

The second restriction is related to whether the softening regime of the AM close to the CDW transition temperature is adiabatic or not in the sense of Refs. 59 and 60. Although the behavior of the AM in $LaTe_3$ near T_c is not accessible experimentally, here we rely on the reported universality of the AM characteristics for several members of the RTe_3 family[46]. (The most noticeable aspect of this universality is the same low-temperature value of the AM frequency $\nu_{\rm AM} \approx 2.2\,{\rm THz}$.) Specifically, experiments suggest that the AM in $TbTe_3$ [see Fig. 3(b,c) in Ref. 70] and $DyTe_3$ [see Fig. 8(a,c) in Ref. 71] softens to zero close to the transition temperature. In Refs. 59 and 60, this regime is called "adiabatic". It is illustrated in Fig. 10a. (Non-adiabatic regime would correspond to the case where the AM does not soften to zero, see Fig. 10b.) Thus, we assume the adiabatic regime for $LaTe_3$ as well. As shown in Fig. 1, such an assumption further confines ω_0 and τ_0 to the region above the dashed line. Together with the previous constraint, this implies that $\tau_0 \lesssim 30\,{\rm fs}$.

Now we note that the Heisenberg uncertainty principle suggests that

$$\tau_0 \gtrsim \frac{1}{2\Delta} \approx 6\,{\rm fs}, \tag{21}$$

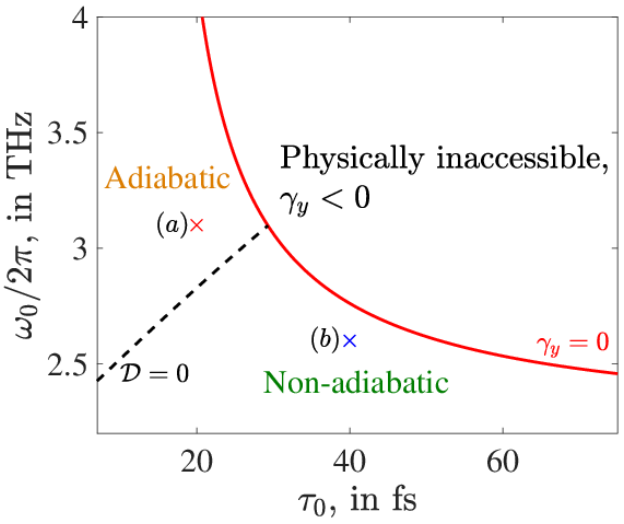

FIG. 1. (Color online) Constraints on the allowed values of the TDGL parameters τ_0 and ω_0 formulated in subsection III A. The area above the solid red curve is physically inaccessible because it corresponds to $\gamma_y(\omega_0, \tau_0) < 0$. The available parameter space to the left and below the solid curve hosts two regimes of small oscillations, adiabatic (above the dashed line) and non-adiabatic (below the dashed line), see subsection III A and Appendix B. These two regimes are exemplified by two points, (a) and (b), for which the mode softening is illustrated in Fig. 10. The dashed line is determined by equation $\mathcal{D} = 0$, where $\mathcal{D}$ is defined by Eq. (B9). The parameters ω_0 and τ_0 for $LaTe_3$ are assumed to represent the adiabatic regime.

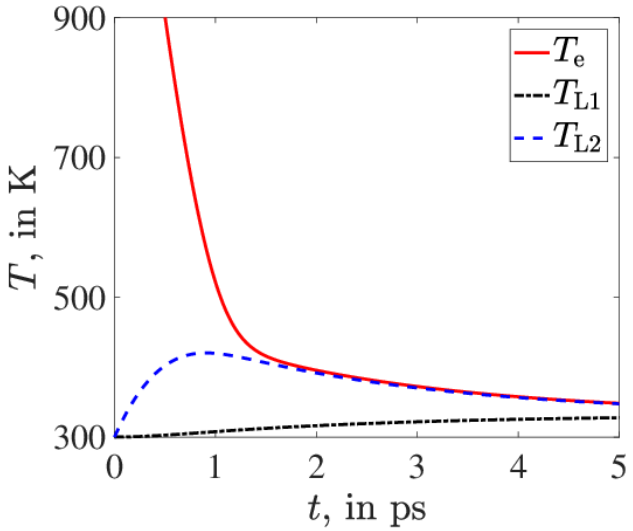

FIG. 2. (Color online) Typical example of the time evolution of electronic temperature (solid red line), temperature of CDW phonons (dashed blue line), and temperature of non-CDW phonons (dotted black line). The curves are computed numerically on the basis of Eqs. (16-18) with the initial value of T_e corresponding to the photoexcitation density $F = 2 \times 10^{20}\,\mathrm{cm}^{-3}$ and with parameters given in Table I.

where the value of the CDW gap is[49] $2\Delta \approx 700\,\mathrm{meV}$ at 300 K.

Keeping the above constraints in mind, we assign $\tau_0 = 20\,\mathrm{fs}$. The outcome of numerical simulations is not too sensitive to specific choice of τ_0.

Finally, to set ω_0 we will use the relation

$$\omega_{\mathrm{AM}}(T = 0) = \lambda_{\mathrm{CDW}}^{1/2}\omega_0, \tag{22}$$

where λ_{CDW} is the electron-phonon coupling constant[72], responsible for the CDW instability. Often, it is assumed [see, e.g., discussion after Eq. (5) in Ref. 25, and Table 3.1 of Ref. 72] that $\lambda_{\mathrm{CDW}} \approx 0.5$. When this value is substituted into Eq. (22), one obtains $\omega_0/(2\pi) \approx 3.1\,\mathrm{THz}$ assuming that Eq. (20) remains a good approximation for $\omega_{\mathrm{AM}}(T)$ even at $T = 0$.

Once τ_0 and ω_0 are determined, both $\gamma_y = \gamma_y(\omega_0, \tau_0)$ and $\zeta = \zeta(\omega_0, \tau_0)$ are obtained. The final values are summarized in Table I.

B. Three-temperature model parameters

Let us start with the discussion of temperature-dependence of $C_e(T_e)$. At sufficiently low temperatures, electronic heat capacity is a linear function of temperature

$$C_e^0(T_e) = c_0 T_e, \tag{23}$$

where[44] $c_0 = 1.1\,\mathrm{mJ/mol\,K^2}$ for $LaTe_3$. In the proximity to and above the phase transition temperature $T_c = 670\,\mathrm{K}$, we do not expect Eq. (23) to remain valid. It would imply that the electronic temperature following the maximum intensity laser pulse reaches the value $\approx 4000\,\mathrm{K}$, while the analysis of our tr-ARPES data presented in Appendix C 2 reveals that $T_e \lesssim 2000\,\mathrm{K}$, see Fig. 13. The deviation from the linear temperature dependence (23) is also expected on the basis of purely theoretical reasoning outlined in Appendix C 1. Therefore, in order to approximate the temperature dependence of $C_e(T_e)$, we adopt the following piecewise linear ansatz

$$C_e(T_e) = \begin{cases} c_0 T_e, & \text{if } T_e < T_{\mathrm{env}}, \\ c_0 T_{\mathrm{env}} + (T_e - T_{\mathrm{env}})c, & \text{if } T_{\mathrm{env}} < T_e, \end{cases} \tag{24}$$

which is further motivated in Appendix C 1. Here $c = 4\,\mathrm{mJ/mol\,K^2}$ is a parameter extracted from tr-ARPES experiments.

Next we discuss lattice heat capacities C_{L1} and C_{L2}, which enter Eqs. (17) and (18). Since both parameters represent heat capacities of two complementary groups of phonons, we will assume

$$C_{L1} = (1 - \kappa)C_{\mathrm{tot}}, \; C_{L2} = \kappa C_{\mathrm{tot}}, \tag{25}$$

where C_{tot} is the total heat capacity of the lattice, and $0 < \kappa < 1$ is the coefficient determining the fraction of

the phonon modes contributing to $C_{\rm L2}$. We approximate $C_{\rm tot}$ by the Dulong-Petit value 99.7 J/(mol K) for $LaTe_3$, which is permissible in the temperature range of interest and consistent with experiment[44]. The value of κ is fixed to be equal to 0.2 in subsection IV B on the basis of our model fitting to the UED Bragg peak intensities.

A typical post-pulse time evolution of the three temperatures within our model is shown in Fig. 2. Here we assume that the initial rise of the electronic temperature occurs on very short time scale which we approximate as instantaneous. The remaining evolution can be divided into two stages. During the first stage, $T_{\rm e}$ relaxes to $T_{\rm L2}$ on the time scale of 1–2 ps. The second stage unfolds for $t \gtrsim 1.5$ ps, where the common temperature of the electrons and the CDW phonons ($T_{\rm e} \approx T_{\rm L2}$) approaches $T_{\rm L1}$ until all three temperatures reach the same value.

For sufficiently strong laser pulses, such that $T_{\rm e}(0) \gg T_{\rm L1,L2}$, the first stage can be accurately described by the approximate equation

$$C_{\rm e}(T_{\rm e})\frac{dT_{\rm e}}{dt} \approx -G_{\rm eL}T_{\rm e}, \tag{26}$$

which is governed by a single parameter $G_{\rm eL}$. Its value can be estimated by assuming that, at high excitation densities, the measured initial decay of the transient reflectivity is controlled by $T_{\rm e}(t)$. This way, we obtain $G_{\rm eL} = 5.5\,{\rm J/(ps{\cdot}K{\cdot}mol)}$, see subsection IV A for further details.

During the second stage, the temperature relaxation process is exponential, characterized by the time constant

$$\tau_{\rm DW} = \kappa(1-\kappa)C_{\rm tot}/G_{\rm LL}. \tag{27}$$

Here, following the notation of Ref. 8, we use the subscript 'DW', which stands for 'Debye-Waller', because the above time constant controls the evolution of the Bragg peak intensity in the late-time regime. Expression (27) can be derived with the help of Eqs. (17) and (18) in the limit $T_{\rm e} = T_{\rm L2}$ (corresponding to $t > 1.5$ ps in Fig. 2). From the measured relaxation of the Bragg peak intensity[8], we have $\tau_{\rm DW} = 2.2$ ps. Thereby, Eq. (27) defines $G_{\rm LL} = 7.25\,{\rm J/(ps{\cdot}K{\cdot}mol)}$.

IV. COMPARISON OF THE EXPERIMENTS WITH THE NUMERICAL SIMULATIONS

In this section, we present the results of the simulations and compare them with the experimental data. The simulation parameters are given in Table I.

A. Comparison to the short-time transient reflectivity measurements

Laser pulse initially excites electronic degrees of freedom, which, in turn, excite the lattice. Both the electrons and the lattice contribute to the change in the transient reflectivity signal. We expect that the monotonically decaying part of the transient reflectivity (measured transient reflectivity with the oscillating contribution from the amplitude mode subtracted[8]) tracks the dynamics of the electronic temperature $T_{\rm e}(t)$.

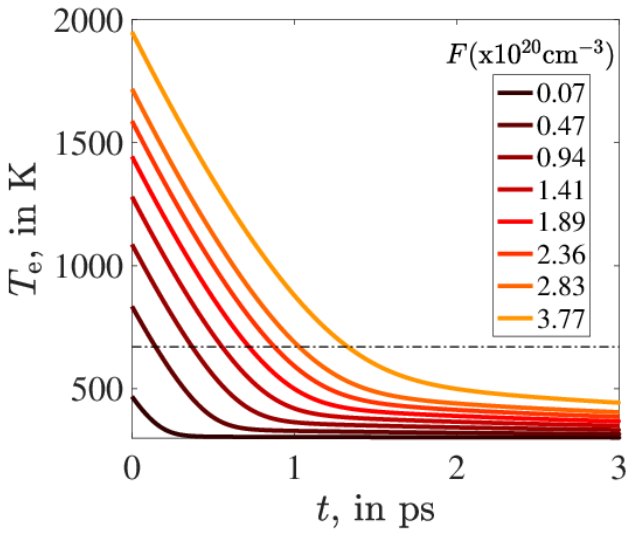

FIG. 3. (Color online) Electronic temperature dynamics for different photoexcitation densities F, as described by the three-temperature model. The in-plot legend explains the correspondence between F and the curves. Horizontal dash-dotted line marks the CDW transition temperature $T_c = 670$ K. The crossing of this line with an individual temperature evolution curve $T_{\rm e}(t)$ defines time $\tau_{T_{\rm c}}(F)$ introduced by Eq. (29).

The computed time dependence $T_{\rm e}(t)$ is shown in Fig. 3 for different excitation densities F. The crossover between the first rapid stage to the second slow stage is clearly seen. For longer times $T_{\rm e}(t)$ approaches some photoexcitation-density-dependent base temperature, which only slightly exceeds $T_{\rm env}$ for all excitation densities used.

To compare the computed temperature evolution with experiment, we introduce time $\tau_{T_{\rm e}}$ by condition

$$T_{\rm e}(\tau_{T_{\rm e}}) - T_{\rm env} = \frac{T_{\rm e}(0) - T_{\rm env}}{e},\ e = 2.718\ldots\ . \tag{28}$$

It characterizes the time scale of the electronic temperature cooling down during the first rapid stage. In Fig. 4, we compare $\tau_{T_{\rm e}}$ with the relaxation time $\tau_{\rm R}$, extracted from the transient reflectivity experiment[8]. Given the simplicity of our model, the agreement between the theory and the experiment is very good. It was attained by adjusting the parameter $G_{\rm eL}$ in Eq. (26), while other parameters affecting the latter equation were fixed as described in subsection III B.

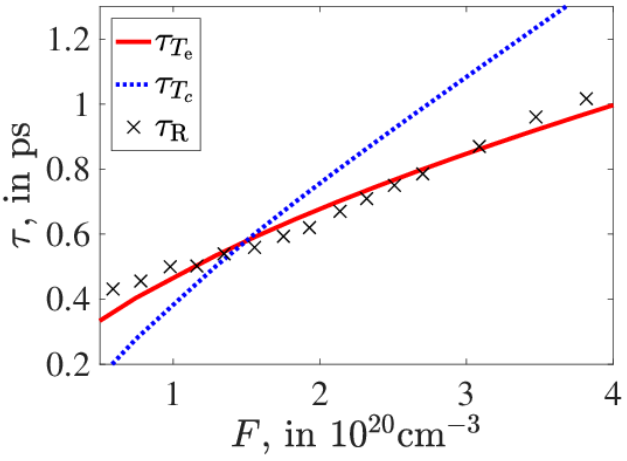

FIG. 4. (Color online) Time scales τ_{T_e}, Eq. (28), and τ_{T_c}, Eq. (29), as functions of photoexcitation density F. Crossed points correspond to the quasiparticle time τ_R, extracted from the transient reflectivity measurements[8].

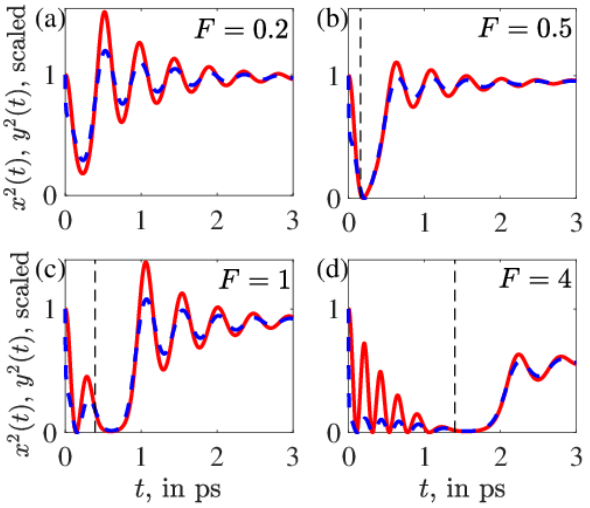

FIG. 5. (Color online) Time evolution of the CDW order parameters. Four panels correspond to different photoexcitation densities F (shown in each panel in units of 10^{20} cm^{-3}). Dashed blue lines show time-dependence of the electronic CDW order $x^2(t)$ normalized to its pre-pulse value $x^2(0^-)$. Similarly, solid red lines show the time evolution of the lattice CDW order represented as $y^2(t)/y^2(0^-)$. Vertical dashed lines mark $t = \tau_{T_c}(F)$ defined by Eq. (29).

B. Dynamics of the order parameters

1. *Melting of the CDW order*

In Fig. 5, the plots of $x^2(t)$ and $y^2(t)$ illustrate the typical dynamics of the electronic and the lattice CDW order parameters after the arrival of a laser pulse. For low excitation densities, such as that of Fig. 5a, the laser pulse never destroys the CDW order as such – it only excites damped AM oscillations around the equilibrium values of the order parameters. For stronger pulses, as in panels (b–d), both $x(t)$ and $y(t)$ cross zero, which, despite the lack of equilibrium, makes one suspect the proximity to the melting of the CDW order.

To investigate the onset of the CDW melting, it is useful to look back at the corresponding temperature evolution $T_e(t)$ shown in Fig. 3, where, indeed, we see that $T_e(t)$ stays above T_c for a finite time. We denote this time as $\tau_{T_c}(F)$. It is defined by condition

$$T_e(\tau_{T_c}) = T_c, \tag{29}$$

which is graphically indicated in Fig. 3 by the dash-dotted horizontal line. For too small F corresponding to $T_e(t)$ never crossing T_c, we define $\tau_{T_c}(F) = 0$. Once F increases above certain threshold, τ_{T_c} grows monotonically with F, as shown in Fig. 4.

In Fig. 5(b–d), the time $t = \tau_{T_c}$ is indicated by vertical dashed lines. We see that τ_{T_c}, indeed, gives the correct estimate of the time ranges when both order parameters cross zero and, hence, are strongly suppressed. We also note that for panel (d), where $\tau_{T_c} \gtrsim 1$ ps, the order parameters demonstrate multiple passages through zero with decreasing amplitude. After the oscillations fade, the order parameters remain suppressed for about 0.5 ps.

In general, the notion of melting in the course of a non-equilibrium evolution is not sharply defined. Here we adopt the criterion that the CDW order undergoes melting when the electronic and the lattice order parameters in the course of their time evolution do not simply cross zero but approach zero in the damped oscillatory (or non-oscillatory) fashion. This criterion implies that the memory of the initial long-range correlations is lost after the system re-emerges from the melting state. From such a prospective, we conclude that Fig. 5d exhibits melting, while Fig. 5b does not, and Fig. 5c is the border case. On the basis of the above analysis, we conclude that the critical excitation density F_c, defined as the lowest border for melting, satisfies the following inequality

$$1 \times 10^{20}\,\text{cm}^{-3} \lesssim F_c < 4 \times 10^{20}\,\text{cm}^{-3}. \tag{30}$$

Experimentally[8] $F_c \sim 2.0 \times 10^{20}$ cm^{-3}, in agreement with the above constraints.

All plots in Fig. 5 exhibit prominent oscillatory behavior of the order parameters. At lower photoexcitation densities, such as in Fig. 5a, the oscillations are clearly related to the appearance of the AM observed in the transient reflectivity experiments. However, the

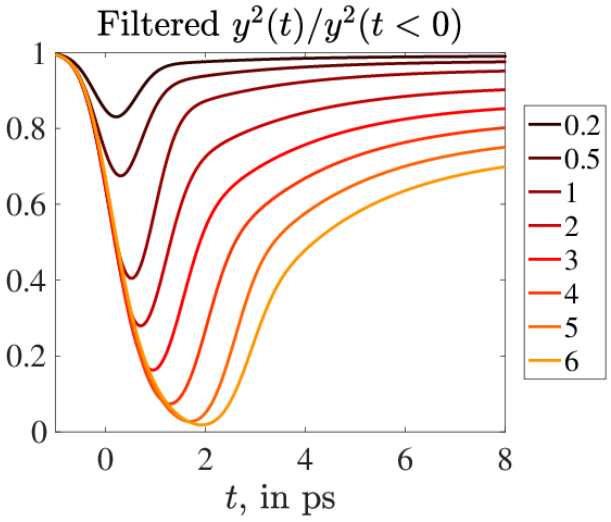

FIG. 6. (Color online) Time evolution of the lattice order parameter $y^2(t)/y^2(t<0)$ – see Fig. 5 – filtered with Gaussian function in Eq. (33) in order to mimic finite resolution in the UED experiment.

experiment indicates significant reduction of the oscillation amplitude for $F \gtrsim 2\times10^{20}\,\mathrm{cm}^{-3}$. This discrepancy can be attributed to our assumption that the order parameters are homogeneous in space, while in the real system, the spatial configuration of the order parameters following the onset of melting and subsequent freezing is likely strongly inhomogeneous due to the appearance of topological defects in the order parameter texture. As a result of this inhomogeneity, the system has relatively small coherent CDW domains of varying size with different size-dependent frequencies ω_0, which, in turn, leads to the strong dephasing of the oscillations, once the signal is averaged over the entire sample.

Further analyzing oscillations in Fig. 5d, we observe that the frequency of transient oscillations for $t \lesssim 1.5\,\mathrm{ps}$ is twice the AM frequency ω_{AM}. Such a doubling occurs because of the interplay of two factors: (i) in Fig. 5 we plot $x^2(t)$ and $y^2(t)$ instead of $x(t)$ and $y(t)$ and (ii) the order parameters oscillate near $x = y = 0$. The experiments of Refs.[62,73] indicate that such a frequency doubling may, actually, occur in real systems.

2. *Two kinds of diffraction peaks in UED experiments*

The UED experiments[8] observe two kinds of diffraction peaks associated either with the underlying crystal order of $LaTe_3$ or with the CDW order, see Fig. 7. The measurements of Ref. 8 were done in the higher-order Brillouin zones, which implies that the measured intensities of the CDW peaks are determined[74] by the lattice CDW order y. Fundamentally, the integrated intensity of a CDW peak is proportional to $|y|^2$. Therefore, at first sight, the direct way to test our modeling

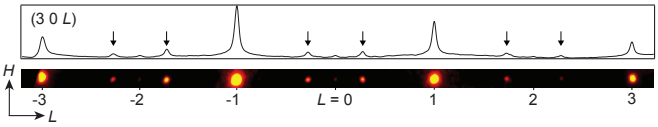

FIG. 7. (Color online) Static electron diffraction pattern along (3 0 L). The line cut is obtained by integrating the colored strip along the H direction. The measured diffraction is a two-dimensional slice in the three-dimensional reciprocal space. The bright yellow spots are Bragg peaks while arrows mark the CDW superlattice peaks. Figure reproduced from Ref. 8.

is to compare the calculated $|y|^2(t)$ with the time evolution of the integrated CDW peak intensity measured in the UED experiment. However, the problem here is that, on the one hand, the CDW peaks are broader than the experimental resolution, while, on the other hand, the experiments measure intensities only for a two-dimensional slice (k_x, k_z) of a three-dimensional reciprocal space (k_x, k_y, k_z), see Fig. 7. Therefore, no direct experimental information about the three-dimensional integrated intensity of the CDW peaks is available to us.

At the same time, since, in the experiment[8], crystal Bragg peaks are resolution-limited, the two-dimensional integrals over the measured sections of these peaks are proportional to the respective integrals over the full three-dimensional reciprocal space. One can now take into account the sum rule implying that the emergence of the CDW order leads to the intensity transfer from the Bragg peaks to the CDW peaks, see Appendix A. Therefore, in our case, the most direct way to extract the value of $|y|^2(t)$ from experiment is to examine the integrated intensity lost by the Bragg peaks.

3. *Time evolution of the Bragg peaks for the underlying crystal lattice from UED experiments*

To model the evolution of the Bragg peak intensity in the presence of the CDW order, we use the expression obtained in Ref. 75:

$$I \propto [J_0(py)]^2 e^{-2W}, \tag{31}$$

where I is the integrated Bragg peak intensity, J_0 is the zeroth order Bessel function, and p is a constant [compare to Eq. (A8)]. Parameter W accounts for the Debye-Waller suppression of the intensity due to thermal fluctuations of the phonons. It is expected that $W \propto T_{\mathrm{L1}}$. Therefore, we have

$$\frac{I(t)}{I(0)} = \frac{J_0(py(t))}{J_0(py(0))} e^{-2[W(t)-W(0)]} \approx \\ \approx 1 - P[y^2(t) - y_{\mathrm{eq}}^2] - S[T_{\mathrm{L1}}(t) - T_{\mathrm{env}}], \tag{32}$$

where $P = p^2/2$, and S is a constant.

To account for experimental temporal resolution, the result in Eq. (32) should be convoluted with the Gaussian

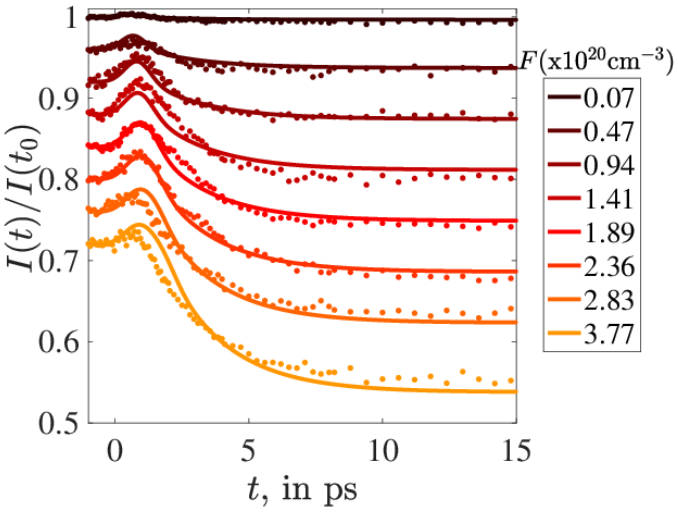

FIG. 8. (Color online) Time evolution of the Bragg peaks intensity $I(t)$ for different excitation densities. Solid lines are obtained from Eq. (34); dots represent the experimental data[8]. The lines and the data points for different excitation densities are vertically displaced for clarity.

filter

$$g(t) = \frac{1}{\sqrt{2\pi}w} \exp\left(-\frac{t^2}{2w^2}\right), \tag{33}$$

where $w \approx 0.42\,\text{ps}$ is the width parameter characterizing the UED experiment of Ref. 8. The resulting quantity $(y^2 * g)(t)$, where the asterisk denotes time convolution, represents filtered dynamics of the lattice order parameter. It is plotted in Fig. 6 for different F's. Notably, the oscillations seen in all panels of Fig. 5 have been smeared out: the resolution of the UED measurements is insufficient to detect them.

Finally, to mimic the actual Bragg peaks dynamics, we use the following expression

$$\frac{I(t)}{I(t_0)} \approx \{1 - P[y^2(t-t_0) - y_{\text{eq}}^2] - S[T_{\text{L1}}(t-t_0) - T_{\text{env}}]\} * g. \tag{34}$$

Here t_0 is an adjustable parameter shifting the origin of the time axis. It originates from the limited time resolution of the experiment. By fitting Eq. (34) to the experiment, we found that $P = 0.1$, $S = 3 \times 10^{-3}$, and $t_0 = 0.43\,\text{ps}$. The resulting functions $I(t)$, together with the UED data points, are plotted in Fig. 8. The agreement between the fits and the experiment is rather good for moderate excitation densities F. For higher F, the small discrepancy might be due to the fact that approximation (24) for the electronic heat capacity is less accurate at higher temperatures.

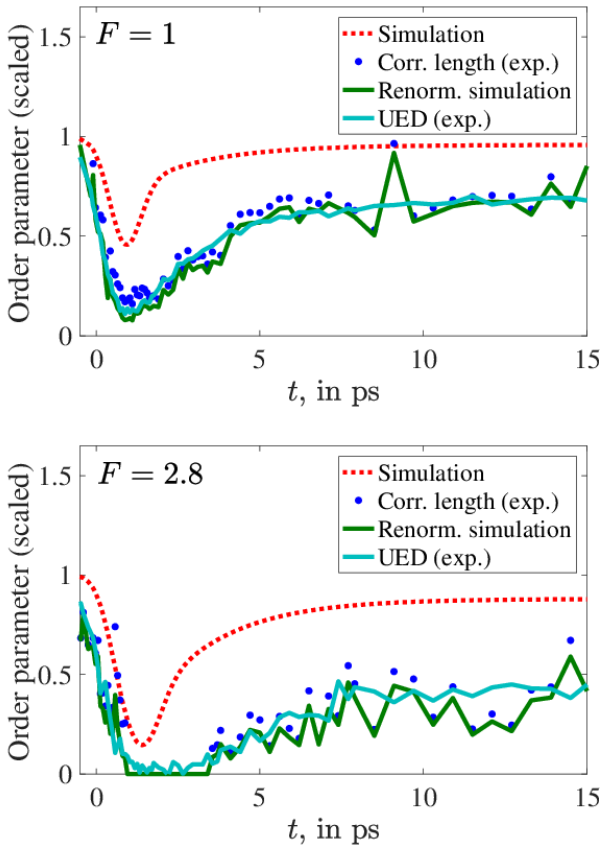

FIG. 9. (Color online) Comparison of the simulated dynamics with the UED data for the CDW peak. Two panels correspond to two different photoexcitation densities: $F = 9.4 \times 10^{19}\,\text{cm}^{-3}$ (top panel) and $F = 2.8 \times 10^{20}\,\text{cm}^{-3}$ (bottom). Quantity $(y^2 * g)(t)$, representing simulated filtered dynamics of the order parameter (see Fig. 6), is shown by dashed (red) curve. Experimentally obtained[8] partially integrated UED intensity I_{2D}^{CDW}, Eq. (37), is shown by solid (cyan) curves. The data points[8] for the CDW correlation length ξ are shown as (blue) dots. For larger F (bottom panel), the CDW peak disappears for $1\,\text{ps} \lesssim t \lesssim 3.5\,\text{ps}$, consequently, the data points for ξ are absent in this interval. To account for the theoretically unknown phase dynamics, we multiply $(y^2 * g)$ by ξ [as in Eq. (40)]. The resulting dependence is shown by solid (green) line. For both F's, the agreement between I_{2D}^{CDW} and $(y^2 * g)\,\xi$ is quite notable.

4. *Time evolution of the CDW peak from UED experiments*

We now turn to the discussion of the CDW peak, which contains information about the long-range lattice order. It tracks both the amplitude and the phase, cf. Eq. (A12). We assume that the intensity of the CDW peak in the reciprocal space can be reasonably approximated by a factorized function

$$\mathcal{G}^{\text{CDW}}(\mathbf{k}) \propto y^2 s_x(k_x) s_y(k_y) s_z(k_z) \tag{35}$$

where $s_\sigma(k_\sigma)$ are the peak shape functions for the respective k-space directions, with index σ taking values x, y,

or z. Axes x and z correspond to the in-plane directions, while axis y is directed out of plane. (The notations x and y for the spatial axes appear only as subscripts, and are not to be confused with the variables x and y defined earlier that represent the electronic and the lattice order.) Functions $s_\sigma(k_\sigma)$ are normalized by the condition

$$\int dk s_\sigma(k) = 1. \tag{36}$$

We also assume that these functions are non-negative and bell-shaped. (In experiment, these functions are fitted by Lorentzians.) The partially integrated intensity of CDW peak reported in Ref. 8 can be written as

$$I_{2D}^{\mathrm{CDW}} \equiv \int dk_x dk_z \mathcal{G}^{\mathrm{CDW}}(\mathbf{k})|_{k_y=0} = y^2 s_y(0). \tag{37}$$

Now we observe that, for common bell-shaped functions, such as Lorentzian or Gaussian, $s_\sigma(0) \propto \xi_\sigma$, where ξ_σ is the real-space correlation length in the respective direction. Using this observation and adding explicit time dependencies of the parameters involved, we arrive at the expression

$$I_{2D}^{\mathrm{CDW}}(t) \propto y^2(t)\xi_y(t). \tag{38}$$

In this work, we assume that the order parameter is homogeneous is space. Thus, we cannot obtain theoretically $\xi_y(t)$. However, we can estimate it on the basis of the assumption that all correlation lengths are determined by the same mechanism and hence are proportional to each other, i.e.

$$\xi_y(t) \propto \xi_{x,z}(t) \approx \xi_{\mathrm{exp}}(t), \tag{39}$$

where $\xi_{\mathrm{exp}}(t)$ is the experimentally measured correlation length in x and z directions, obtained as the inverse of the FWHM of the CDW peak after instrumental resolution is taken into consideration, see Eq. (S4) of the Supplementary Information to Ref. 8.

Finally, taking into account the limited experimental time resolution described by function g from Eq. (33), the experimentally measured integrated intensity can be expressed as $I_{2D,\mathrm{exp}}^{\mathrm{CDW}}(t) \propto [(y^2\xi_{\mathrm{exp}})*g](t) \approx (y^2*g)(t)\,\xi_{\mathrm{exp}}(t)$. To facilitate the comparison with experiments, we re-express this relation as

$$\frac{I_{2D,\mathrm{exp}}^{\mathrm{CDW}}(t)}{I_{2D,\mathrm{exp}}^{\mathrm{CDW}}(0^-)} = \frac{(y^2*g)(t)\,\xi_{\mathrm{exp}}(t)}{(y^2*g)(0^-)\,\xi_{\mathrm{exp}}(0^-)}, \tag{40}$$

where the argument (0^-) implies the pre-pulse values of the respective parameters.

In Fig. 9, we test the relation (40) by substituting there the theoretically calculated $y^2(t)$. The latter function is shifted by $t_0 = 0.43\,\mathrm{ps}$ to properly place the time origin, see the text following Eq. (34). The agreement between the lines representing the left-hand side and the right-hand side of Eq. (40) is rather encouraging, thereby representing another consistency check of our modeling.

V. DISCUSSION AND CONCLUSIONS

In this paper, we used the time-dependent Ginzburg-Landau equations, supplemented by the three-temperature model, to describe the dynamics of the CDW order parameter amplitude in a photo-induced transition, and applied it to the pump-probe experiments in $LaTe_3$. With this formalism, we were able to reproduce several features of the UED and transient reflectivity experiments of Ref. 8. Among the successes of our modeling are (i) the simulation of the Bragg peak intensity evolution presented in Fig. 8, where all eight data sets were fitted with a small number of adjustable parameters, and (ii) the agreement between the simulated electronic temperature relaxation and the transient reflectivity experiments, see Figs. 3 and 4. In addition, we were able to reach the agreement between the measured and simulated intensity evolution for the UED CDW peak, by taking into account the CDW peak broadening, see Fig. 9.

The above successes are rooted in several features of the proposed model. Unlike a classical TDGL equation, we employed the two-parameter TDGL formalism, which treats separately the dynamics of lattice deformation u and electronic density A. With a single-parameter TDGL, it is difficult, if not impossible, to approximate the initial evolution of the photo-excited state. Furthermore, the introduction of unequal temperatures for the electrons and the lattice is another essential element of our modeling.

As far as the limitations of our modeling are concerned, it is worth mentioning that many CDW systems demonstrate pronounced non-mean-field thermodynamics properties near the phase transition[30–32]. This applies to our compound $LaTe_3$ as well: due to its quasi-two-dimensional character, it is obviously affected by non-mean-field order parameter fluctuations. In a related argument, we proposed in Ref. 8 that topological excitations influence the long-time dynamics of our system. The above considerations emphasize the role played by the spatially inhomogeneous phase fluctuations of the CDW order parameter. In the present work, our numerical simulations ignored the phase fluctuations of the order parameters, focusing entirely on their amplitudes, see subsection IV B 2.

Another limitation is related to the use of the three-temperature model, which greatly oversimplifies the kinetic processes in the studied system. However, our success in reproducing the experiments in general and, the transient reflectivity experiments in particular, suggests that this approximation captures essential physics of the system.

VI. ACKNOWLEDGEMENTS

We thank T. Rohwer, C. Lee, E. J. Sie, E. Baldini, B. Freelon, and H. Zhou for the help in building and

acquiring data from the ultra-fast electron diffraction and time-resolved ARPES setups. We acknowledge high-quality samples prepared by J. Straquadine, P. Walmsley, I. R. Fisher, Y.-Q. Bie, and P. Jarillo-Herrero. All authors acknowledge the support of the Skoltech NGP Program (Skoltech-MIT joint project) (theory). N.G., A.Z., and A.K. also acknowledge the support from the Gordon and Betty Moore Foundations EPiQS Initiative grant GBMF4540 (data analysis).

Appendix A: Bragg and CDW peaks

The purpose of this Appendix is to illustrate how the presence of the CDW modifies electron diffraction peaks. We then discuss the role of fluctuations of the phase of the order parameter. The discussion here is a simplified version of a more general treatment of Ref. 75.

We express modulation of the lattice site positions as

$$\mathbf{r}_n \to \mathbf{r}_n + \mathbf{u}\cos(\mathbf{Q}\cdot\mathbf{r}_n), \tag{A1}$$

where $\mathbf{u}$ and $\mathbf{Q}$ are the amplitude and the wave vector of the modulation; $\mathbf{r}_n$ are high-symmetry lattice points. Assuming that the amplitude $|\mathbf{u}|$ is much smaller than the lattice spacing, we write the density as

$$\begin{aligned}\rho(\mathbf{r}) &= \sum_{\mathbf{r}_n}\delta\left[\mathbf{r}-\mathbf{r}_n-\mathbf{u}\cos(\mathbf{Q}\cdot\mathbf{r}_n)\right]\approx\\ &\approx \rho_0(\mathbf{r}) - \sum_{\mathbf{r}_n}(\mathbf{u}\cdot\nabla_{\mathbf{r}})\delta(\mathbf{r}-\mathbf{r}_n)\cos(\mathbf{Q}\cdot\mathbf{r}_n)+\\ &+\frac{1}{2}\sum_{\mathbf{r}_n}(\mathbf{u}\cdot\nabla_{\mathbf{r}})^2\delta(\mathbf{r}-\mathbf{r}_n)\cos^2(\mathbf{Q}\cdot\mathbf{r}_n)+\ldots\end{aligned} \tag{A2}$$

where $\rho_0(\mathbf{r}) = \sum_{\mathbf{r}_n}\delta(\mathbf{r}-\mathbf{r}_n)$ corresponds to the density of unmodulated lattice. By performing the Fourier transformation we obtain:

$$\begin{aligned}\rho_{\mathbf{k}} = \rho_{0\mathbf{k}} &- \int d^3\mathbf{r}e^{-i\mathbf{k}\cdot\mathbf{r}}\sum_{\mathbf{r}_n}(\mathbf{u}\cdot\nabla_{\mathbf{r}})\delta(\mathbf{r}-\mathbf{r}_n)\cos(\mathbf{Q}\cdot\mathbf{r}_n)+\\ &+\frac{1}{2}\int d^3\mathbf{r}e^{-i\mathbf{k}\cdot\mathbf{r}}\sum_{\mathbf{r}_n}(\mathbf{u}\cdot\nabla_{\mathbf{r}})^2\delta(\mathbf{r}-\mathbf{r}_n)\cos^2(\mathbf{Q}\cdot\mathbf{r}_n)+\ldots\end{aligned} \tag{A3}$$

where $\rho_{0\mathbf{k}} = F_{\mathbf{k}}\sum_{\mathbf{b}}\delta_{\mathbf{k},\mathbf{b}}$ is a sum of sharp peaks located at reciprocal wave vectors $\mathbf{b}$ of the underlying crystal lattice. Here $F_{\mathbf{k}}$ is the lattice form-factor. Integrating by parts, we obtain

$$\begin{aligned}\rho_{\mathbf{k}} = \rho_{0\mathbf{k}} &- i(\mathbf{u}\cdot\mathbf{k})\sum_{\mathbf{r}_n}e^{-i\mathbf{k}\cdot\mathbf{r}_n}\cos(\mathbf{Q}\cdot\mathbf{r}_n)-\\ &-\frac{(\mathbf{u}\cdot\mathbf{k})^2}{4}\sum_{\mathbf{r}_n}e^{-i\mathbf{k}\cdot\mathbf{r}_n}\left[1+\cos(2\mathbf{Q}\cdot\mathbf{r}_n)\right]+\ldots\end{aligned} \tag{A4}$$

The terms in Eq. (A4) can be combined as follows:

$$\rho_{\mathbf{k}} = \left[1-\frac{(\mathbf{u}\cdot\mathbf{k})^2}{4}\right]\rho_{0\mathbf{k}} + \rho^{\mathbf{Q}}_{\mathbf{k}} + \rho^{2\mathbf{Q}}_{\mathbf{k}} + \ldots \tag{A5}$$

where

$$\begin{aligned}\rho^{\mathbf{Q}}_{\mathbf{k}} &= -i(\mathbf{u}\cdot\mathbf{k})\sum_{\mathbf{r}_n}e^{-i\mathbf{k}\cdot\mathbf{r}_n}\cos(\mathbf{Q}\cdot\mathbf{r}_n) =\\ &= -\frac{i}{2}(\mathbf{u}\cdot\mathbf{k})F_{\mathbf{k}}\sum_{\mathbf{b}}(\delta_{\mathbf{k},\mathbf{b}+\mathbf{Q}}+\delta_{\mathbf{k},\mathbf{b}-\mathbf{Q}}),\end{aligned} \tag{A6}$$

$$\begin{aligned}\rho^{2\mathbf{Q}}_{\mathbf{k}} &= -\frac{(\mathbf{u}\cdot\mathbf{k})^2}{4}\sum_{\mathbf{r}_n}e^{-i\mathbf{k}\cdot\mathbf{r}_n}\cos(2\mathbf{Q}\cdot\mathbf{r}_n) =\\ &= -\frac{(\mathbf{u}\cdot\mathbf{k})^2}{8}F_{\mathbf{k}}\sum_{\mathbf{b}}(\delta_{\mathbf{k},\mathbf{b}+2\mathbf{Q}}+\delta_{\mathbf{k},\mathbf{b}-2\mathbf{Q}}).\end{aligned} \tag{A7}$$

These terms describe appearance of the CDW peaks with wave-vectors $n\mathbf{Q}, n = 1, 2, \ldots$

Of particular interest to us is the first term in Eq. (A5). We note that the presence of the CDW suppresses the amplitudes of the Bragg peaks by an amount

$$\delta\rho^{\text{Bragg}}_{\mathbf{k}} = -\frac{(\mathbf{u}\cdot\mathbf{k})^2}{4}\rho_{0\mathbf{k}}. \tag{A8}$$

We use this relation in Sec. IV B.

It is important for our analysis that Eq. (A8) remains valid also when CDW correlations are only short-ranged, while the true long-range CDW order is absent. To show this, we consider more general expression for the ionic density:

$$\rho(\mathbf{r}) = \sum_{\mathbf{r}_n}\delta\left[\mathbf{r}-\mathbf{r}_n-\mathbf{u}\cos(\mathbf{Q}\cdot\mathbf{r}_n+\phi(\mathbf{r}_n))\right]. \tag{A9}$$

Here $\phi(\mathbf{r}_n)$ is the phase of the order parameter. We assume that ϕ is a slowly varying function of $\mathbf{r}_n$. These variations are often referred to as "phasons". In the language of the present paper, they are called "CDW phonons". When $\phi(\mathbf{r}_n)$ varies as a function of $\mathbf{r}_n$, the CDW order weakens, or disappears completely, and becomes replaced by short-range correlations. Generalizing

Eq. (A4) to account for the CDW phonons, we derive

$$\rho_{\mathbf{k}} = \left[1 - \frac{(\mathbf{u}\cdot\mathbf{k})^2}{4}\right]\rho_{0\mathbf{k}} - i(\mathbf{u}\cdot\mathbf{k})\sum_{\mathbf{r}_n} e^{-i\mathbf{k}\cdot\mathbf{r}_n}\cos(\mathbf{Q}\cdot\mathbf{r}_n + \phi(\mathbf{r}_n)) - \frac{(\mathbf{u}\cdot\mathbf{k})^2}{4}\sum_{\mathbf{r}_n} e^{-i\mathbf{k}\cdot\mathbf{r}_n}\cos(2\mathbf{Q}\cdot\mathbf{r}_n + 2\phi(\mathbf{r}_n)). \tag{A10}$$

Thus, in the presence of the phase variation $\phi(\mathbf{r}_n)$ the amplitudes of the Bragg peaks remain unchanged, c.f. Eq. (A5), while the CDW amplitudes $\rho_{\mathbf{k}}^{\mathbf{Q}}$ and $\rho_{\mathbf{k}}^{2\mathbf{Q}}$ become equal to

$$\rho_{\mathbf{k}}^{\mathbf{Q}} = -i(\mathbf{u}\cdot\mathbf{k})\sum_{\mathbf{r}_n} e^{-i\mathbf{k}\cdot\mathbf{r}_n}\cos(\mathbf{Q}\cdot\mathbf{r}_n + \phi(\mathbf{r}_n)), \tag{A11}$$

$$\rho_{\mathbf{k}}^{2\mathbf{Q}} = -\frac{(\mathbf{u}\cdot\mathbf{k})^2}{4}\sum_{\mathbf{r}_n} e^{-i\mathbf{k}\cdot\mathbf{r}_n}\cos(2\mathbf{Q}\cdot\mathbf{r}_n + 2\phi(\mathbf{r}_n)). \tag{A12}$$

We, therefore, conclude that the CDW-induced changes in the Bragg peaks intensities carry information about the short-range CDW correlations. In particular, by means of Eq. (A8) one can extract the amplitude u experimentally.

Appendix B: Small oscillations near equilibrium state

The TDGL sector of our formalism, Eqs. (12) and (15), contains several unknown coefficients. An important part of our study is the evaluation of these parameters consistent with the available data. An interesting possibility in this regard is to investigate the regime of small oscillations of x and y near the equilibrium state. The resulting theoretically determined frequency and damping factor can be compared with experimental data for the AM oscillation spectrum, which allows us to recover several parameters of our model. Since the calculations for $T < T_c$ and $T > T_c$ differ, they will be presented separately.

1. Oscillations for $T < T_c$

When $T < T_c$, both order parameters x and y have non-zero values at equilibrium. In this regime, we parameterize small oscillations as

$$x = \sqrt{\Theta} + \delta x, \quad y = \sqrt{\Theta} + \delta y, \tag{B1}$$

where both δx and δy are complex variables. Writing δx and δy as sums of real and imaginary parts $\delta x = \delta x' + i\delta x''$ and $\delta y = \delta y' + i\delta y''$, we derive the following system of linearized equations

$$\tau_0\frac{d\delta x'}{dt} + 2\Theta\delta x' + \zeta(\delta x' - \delta y') = 0, \tag{B2}$$

$$\frac{1}{\omega_0^2}\frac{d^2\delta y'}{dt^2} + \frac{\gamma_y}{\omega_0}\frac{d\delta y'}{dt} + (\delta y' - \delta x') = 0, \tag{B3}$$

$$\tau_0\frac{d\delta x''}{dt} + \zeta(\delta x'' - \delta y'') = 0, \tag{B4}$$

$$\frac{1}{\omega_0^2}\frac{d^2\delta y''}{dt^2} + \frac{\gamma_y}{\omega_0}\frac{d\delta y''}{dt} + (\delta y'' - \delta x'') = 0. \tag{B5}$$

In these equations, the dynamics of the real and imaginary components are decoupled from each other.

We analyze first the frequencies of the real components in Eqs. (B2) and (B3). The insertion of an ansatz $\delta x'(t) = Xe^{\lambda t}$ and $\delta y'(t) = Ye^{\lambda t}$ leads to an equation for λ:

$$P(\lambda) = 0, \tag{B6}$$

where $P(\lambda)$ is a cubic polynomial defined as

$$P(\lambda) = \tau_0\lambda^3 + (2\Theta + \zeta + \gamma_y\omega_0\tau_0)\lambda^2 + \omega_0(2\Theta\gamma_y + \zeta\gamma_y + \omega_0\tau_0)\lambda + 2\Theta\omega_0^2. \tag{B7}$$

Among three roots of $P(\lambda)$, one is always real and negative. Dependent on parameters, two other roots are either (i) both complex and conjugated to each other, or (ii) both real negative. In case (i), the pair of complex roots represents AM. We identify $\mathrm{Im}\lambda$ with the frequency ω_{AM}, while $-\mathrm{Re}\lambda$ is the AM damping parameter γ_{AM}. The calculated values of ω_{AM} and γ_{AM}, as functions of temperature, are plotted in Fig. 10.

Examining panels (a) and (b) of Fig. 10 we notice that the temperature dependence of the AM exhibits two different qualitative regimes determined by the model parameters. Frequency ω_{AM} plotted in panel (a) remains zero in some finite vicinity of T_c. As for panel (b), ω_{AM} never vanishes. Following Refs. 59 and 60, where this dichotomy was previously analyzed, we refer to the behavior shown in panel (a) of Fig. 10 as "adiabatic", while the one shown is in panel (b) is to be called "non-adiabatic".

To determine the border between the adiabatic and non-adiabatic regimes, we need to analyze ω_{AM} at $T = T_c$. This condition corresponds to $\Theta = 0$. As a result, Eq. (B6) becomes easily solvable:

$$\lambda_1 = 0, \quad \lambda_{2,3} = -\frac{1}{2\tau_0}\left[\gamma_y\omega_0\tau_0 + \zeta \pm \sqrt{\mathcal{D}}\right], \tag{B8}$$

where

$$\mathcal{D} = (\gamma_y\omega_0\tau_0 - \zeta)^2 - 4(\omega_0\tau_0)^2. \tag{B9}$$

Quantity $\mathcal{D}$ is important for our analysis. Specifically, Eq. (B8) implies that, if $\mathcal{D} > 0$, then $\omega_{\mathrm{AM}} = 0$, otherwise, it is finite: $\omega_{\mathrm{AM}} = |\mathrm{Im}\lambda_{2,3}| = \frac{1}{2\tau_0}\sqrt{-\mathcal{D}}$. Therefore, the condition $\mathcal{D} = 0$ separates the adiabatic and non-adiabatic regimes. (In terms of experiment, it might be difficult to detect the difference between a formally adiabatic case $\omega_{\mathrm{AM}}(T = T_c) = 0$, and a non-adiabatic case

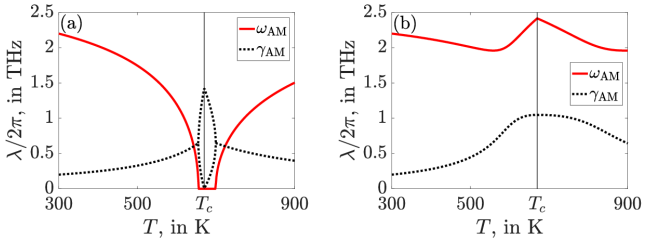

FIG. 10. (Color online) Temperature dependence of the amplitude mode frequency $\omega_{\rm AM}$ and damping parameter $\gamma_{\rm AM}$ obtained by solving Eqs. (B6), (B7). (a) Adiabatic regime: the parameters in Eq. (B7) are $\omega_0/(2\pi) = 3.1\,$THz, $\tau_0 = 20\,$fs, $\zeta \approx 1.1$, and $\gamma_y \approx 0.04$. These parameter values were used in our simulations, see Table I. They correspond to point (a) marked in Fig. 1. In a small temperature range around T_c, the amplitude oscillation mode turns into two overdamped modes with $\omega_{\rm AM} = 0$ and unequal values of $\gamma_{\rm AM}$ represented by two split dashed lines. (b) Non-adiabatic regime: the parameters in Eq. (B7) are $\omega_0/(2\pi) = 2.6\,$THz, $\tau_0 = 40\,$fs, $\zeta \approx 0.5$, and $\gamma_y \approx 0.033$. This choice of parameters corresponds to point (b) marked in Fig. 1.

characterized by inequality $\gamma_{\rm AM}(T = T_c) \gg \omega_{\rm AM}(T = T_c)$.)

Since the values of $\omega_{\rm AM}$ and $\gamma_{\rm AM}$ at $T = 300\,$K are known from experiment, see Eq. (20), we can use them to derive constraints on the TDGL parameters. To obtain the constraints, we re-write Eq. (B6) as two real-valued equations

$$\mathrm{Re}\, P(i\omega_{\rm AM} - \gamma_{\rm AM}) = 0, \tag{B10}$$
$$\mathrm{Im}\, P(i\omega_{\rm AM} - \gamma_{\rm AM}) = 0. \tag{B11}$$

These equations reduce the number of free TDGL coefficients from four (ω_0, τ_0, ζ, and γ_y) to two. In the main text, we treat τ_0 and ω_0 as free parameters. Within such a convention, Eqs. (B10) and (B11) can be used to define two implicit functions $\gamma_y = \gamma_y(\omega_0, \tau_0)$ and $\zeta = \zeta(\omega_0, \tau_0)$.

Damping parameter γ_y must always be non-negative, i.e.

$$\gamma_y(\omega_0, \tau_0) \geq 0, \tag{B12}$$

which further limits the available space for ω_0 and τ_0 as discussed in the main text, see also Fig. 1.

Now we can analyze Eqs. (B4)–(B5), which describe the oscillations of the imaginary components $\delta x''$ and $\delta y''$. One can check that, in this case, we also have three modes whose eigenfrequencies are given by Eq. (B8). The zero eigenfrequency represents a Goldstone mode. Within our model small oscillations of $\delta x''$ and $\delta y''$ have temperature-independent frequencies and damping parameters. This is a consequence of our assumption that quantity a in the Landau functional (3) is the only one dependent on temperature.

As with the real components, the dynamics of the imaginary components $\delta x''$ and $\delta y''$ is sensitive to the sign of $\mathcal{D}$. Specifically, in the adiabatic regime, the roots $\lambda_{2,3}$ are both real negative, i.e. the time evolution is overdamped. In the non-adiabatic regime, the roots form a complex conjugate pair, which corresponds to underdamped oscillations.

2. Oscillations for $T > T_c$

When $T \geq T_c$, the equilibrium values of x and y are zero. Thus, in the regime of linear oscillations in the disordered phase one writes $x(t) = \delta x(t)$ and $y(t) = \delta y(t)$. The resulting linearized equations for the real components coincide with the equations for the imaginary components:

$$\tau_0 \frac{d\delta x}{dt} - \Theta \delta x + \zeta(\delta x - \delta y) = 0, \tag{B13}$$
$$\frac{1}{\omega_0^2}\frac{d^2\delta y}{dt^2} + \frac{\gamma_y}{\omega_0}\frac{d\delta y}{dt} + (\delta y - \delta x) = 0. \tag{B14}$$

The eigenfrequencies then satisfy the equation

$$\tau_0\lambda^3 + (\zeta - \Theta + \gamma_y\omega_0\tau_0)\lambda^2 + \omega_0(\gamma_y\zeta - \gamma_y\Theta + \omega_0\tau_0)\lambda - \Theta\omega_0^2 = 0. \tag{B15}$$

Naturally, at the transition ($\Theta = 0$), Eq. (B15) and Eq. (B6) are identical. This ensures that all eigenfrequencies smoothly cross T_c. Figure 10 shows the numerically calculated eigenfrequencies for both adiabatic and non-adiabatic regimes.

Appendix C: Electronic heat capacity

1. Temperature dependence of the electronic heat capacity

Here we further motivate Eq. (24) for the temperature dependence of the electronic heat capacity. We already mentioned that $LaTe_3$, despite the presence of the CDW order, is not an insulator, but rather is a metal, with ungapped fragments of the Fermi surface and finite density of states at the Fermi energy $\epsilon_F = 0$, cf. Fig. 13. Consequently, the low-temperature heat capacity demonstrates[44] metallic behavior expressed by Eq. (23). However, unlike a "classical" metal for which deviations from linear relation $C_{\rm e} \propto T_{\rm e}$ for $T_{\rm e} \lesssim 2000\,$K are generally weak[76], we expect that the CDW order in $LaTe_3$ affects the validity of Eq. (23) in the above temperature range.

Available thermodynamic and *ab initio* data support[44] this expectation: the CDW order suppresses coefficient c_0 in Eq. (23) almost twofold relative to its value in the hypothetical situation without the CDW order. We assume that this suppression is due to the "pseudo-gapped" single-electron density of state (DOS) $\nu(\epsilon)$ sketched in Fig. 11. In this sketch, the uniform metallic DOS ν_0 is modified by the presence of the CDW order. At the Fermi energy ϵ_F, we choose it for concreteness to be two times smaller than the bare value ν_0. This suppression is caused

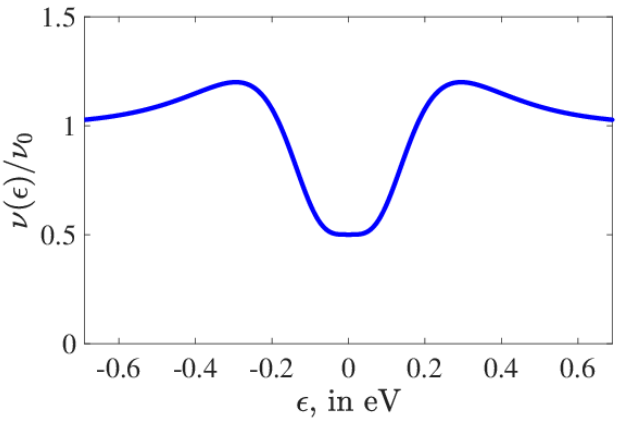

FIG. 11. Normalized DOS in the CDW state. Fermi surface has both metallic and gaped regions. The later states result in (i) the suppression of the DOS at $\epsilon_F = 0$ and (ii) the appearance of maximum around $|\varepsilon| \sim \Delta \sim 350\,\text{meV}$.

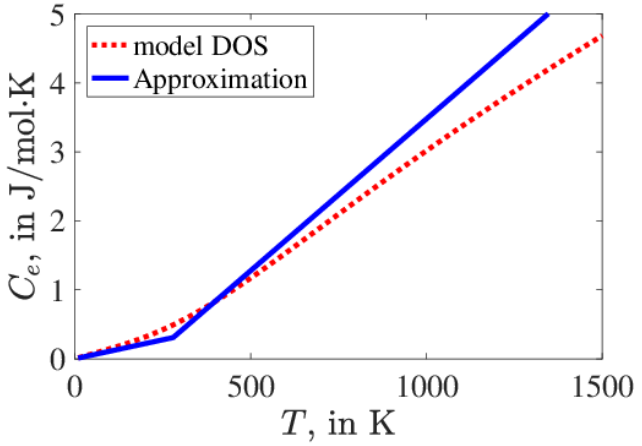

FIG. 12. Dashed (red) line represents temperature dependence of the electronic heat capacity for the DOS shown in Fig. 11. Solid (blue) line corresponds to our approximation Eq. (23).

by the expulsion of the electronic states from the gapped parts of the Fermi surface to higher energies. Since coefficient $c_0 \propto \nu(\epsilon_F)$, the value of c_0 decreases together with $\nu(\epsilon_F)$. As for the states excluded from the vicinity of ϵ_F, they accumulate at[49] $|\epsilon - \epsilon_F| \sim \Delta \sim 0.35\,\text{eV}$. When $|\epsilon - \epsilon_F| \gtrsim 0.6\,\text{eV}$, the DOS returns to its bare value ν_0. The resulting function $\nu(\epsilon)$ exhibits pronounced variations on the scale of hundreds of meV, which leads to a non-linear temperature-dependence of the heat capacity shown in Fig. 12. This temperature dependence is calculated using the expression:

$$C_\text{e}(T_\text{e}) = \int_{-\infty}^{+\infty} \frac{\nu(\varepsilon)\varepsilon^2 d\varepsilon}{2T_\text{e}^2 \cosh^2(\varepsilon/(2T_\text{e}))}. \qquad \text{(C1)}$$

The plot in Fig. 12 indicates that $C_\text{e}(T_\text{e})$ departs from the low-temperature linear dependence, Eq. (23), for $T \gtrsim$

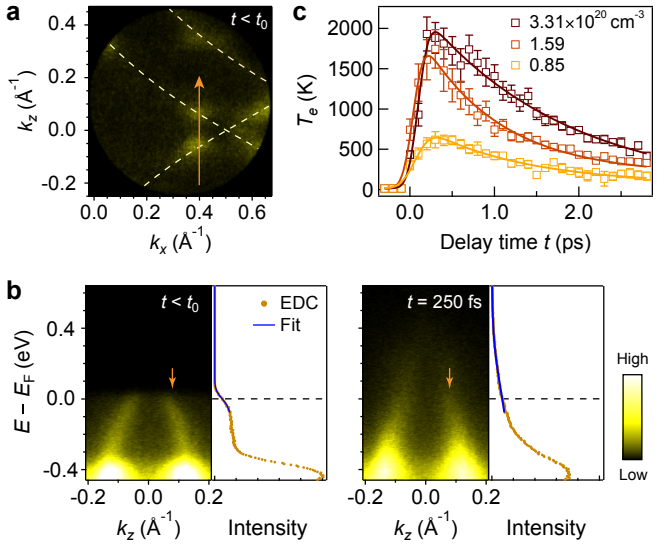

FIG. 13. (Color online) Estimating electronic temperature T_e after a photoexcitation. (a) Fermi surface map before arrival of a laser pulse ($t < t_0$). Intensities are integrated over $\pm 10\,\text{meV}$ around the Fermi energy ϵ_F. Dashed curves represent calculated Fermi surface based on a tight-binding model[77], in the absence of the CDW order. The arrow marks the energy-momentum cut through the ungapped part of the Fermi surface displayed in (b). In (b), the band dispersions are shown at two representative pump-probe time delays: before the laser pulse (left) and 250 fs after the pulse arrival (right). The energy-distribution curves (EDCs) are obtained by integrating over a window $\Delta k = 0.05\,\text{Å}^{-1}$ at the momentum indicated by the arrow. Blue curve is a fit by Eq. (C2) to a part of the EDC. The Fermi energy is indicated by the dashed line. Data in (a) and (b) were obtained at a photoexcitation density of $3.31 \times 10^{20}\,\text{cm}^{-3}$. (c) Electronic temperature T_e plotted as a function of the pump-probe delay for the three photoexcitation densities indicated in the plot legend. Curves are the fits to a single-exponential decay model[8]. Error bars represent one standard deviation of the fits.

300 K. Figure 12 also shows the plot of $C_\text{e}(T_\text{e})$ for a simple piecewise linear function given by Eq. (24). It can be seen in this figure that Eq. (24) adequately approximates $C_\text{e}(T_\text{e})$ in the temperature range of interest.

We note that expression (C1) is formulated under the assumption that $\nu(\varepsilon)$ is independent of T_e. This assumption is, likely, violated in $LaTe_3$, because the actual DOS is sensitive to the values of the order parameters x and y, both of which are temperature- and time-dependent quantities. Thus, application of Eq. (24) to the non-equilibrium situations should be taken with caution. However, we do expect that the piecewise linear function Eq. (24) would still constitute a reasonable approximation to the actual temperature dependence of the electronic heat capacity. Let us also emphasize that accurate knowledge of the electronic heat capacity is important only during the first rapid stage of the electronic temperature relaxation. At the second slow stage, only lattice contributions to the heat capacity are relevant, see

Eq. (27).

2. Estimate of electronic temperature from tr-ARPES

The generation of hot carriers after strong photoexcitation is followed by thermalization within the electronic subsystem on a timescale $\lesssim 100\,\mathrm{fs}$[78]. Using time- and angle-resolved photoemission spectroscopy (tr-ARPES), one can estimate the electronic temperature after the initial thermalization by fitting the energy distribution of quasiparticles to a Fermi-Dirac distribution[79].

Figure 13a shows the Fermi surface in $LaTe_3$ at $T = 15\,\mathrm{K} \ll T_c$ before the arrival of the pump laser pulse (see Ref. 8 for measurement details). The tr-ARPES intensity is absent for the most parts of the Fermi surface due to the opening of the CDW gap. The remaining Fermi surface is consistent with the previous reports[77,80]. In order to minimize complications arising from the transient suppression of the CDW gap, we focus on the ungapped part of the Fermi surface at equilibrium. In Fig. 13b, we present an energy-momentum cut through the metallic part of the Fermi surface where the Te $5p_x/p_z$ bands cross the Fermi level ϵ_F. The same cut is shown after photoexcitation at a pump-probe time delay of $t = 250\,\mathrm{fs}$, where states above ϵ_F are transiently populated.

To quantitatively analyze the carrier redistribution after photoexcitation, we plot the energy distribution curves (EDCs) at $k_z = 0.08\,\mathrm{Å}^{-1}$ indicated by the arrow in Fig. 13b. At $t < t_0$, there is a sharp cutoff of EDC around ϵ_F; this feature is replaced by a long tail at $\epsilon > \epsilon_F$ at 250 fs. The temporal evolution of the EDC across ϵ_F can be captured by the following model[79,81]:

$$I(\epsilon, t) = \{\nu(\epsilon) f[\epsilon, \mu(t), T_\mathrm{e}(t)]\} * \tilde{g}[\epsilon, \tilde{w}(t)], \qquad \text{(C2)}$$

where $\nu(\epsilon)$ is the density of states, $f[\cdot]$ is the Fermi-Dirac distribution that depends on the chemical potential μ and the electronic temperature T_e. The terms in $\{\cdot\}$ are energy convoluted with a Gaussian kernel $\tilde{g}[\cdot]$, cf. Eq. (33), whose time-dependent[79,82] width parameter $\tilde{w}(t)$ arises from the finite energy resolution of the instrument and from spectral broadening due to increased scattering rate after photoexcitation. The density of states $\nu(\epsilon)$ is assumed to remain unchanged over time; it is determined by the EDCs before photoexcitation. This assumption is largely justified, because that particular part of the Fermi surface is minimally affected by the transient suppression and recovery of the CDW gap. To limit the number of free parameters, we adopt a linear approximation $\nu(\epsilon) \approx \nu(\epsilon_\mathrm{F}) + (\epsilon - \epsilon_\mathrm{F})\alpha_\nu$, where α_ν is an adjustable parameter. This, in turn, limits the fitting range as indicated in Fig. 13b, since the strong intensity of a separate band at high binding energy cannot be captured with a linear density of states. In summary, the time-dependent fitting parameters include $\mu(t)$, $T_\mathrm{e}(t)$, and $\tilde{w}(t)$; the value of T_e before the arrival of the laser pulse is fixed to be 15 K, which is the base temperature of the sample during the measurement.

Figure 13c shows the extracted T_e throughout the photoexcitation event for three different excitation densities given in terms of the number of absorbed photons per unit volume. Though electronic temperature obtained within a few τ_0 after photoexcitation is less reliable due to the non-thermal nature of the carrier distribution[78], values at longer time delays are indicative of the quasi-thermal state of the electronic subsystem with effective electronic temperature T_e and a Fermi-Dirac distribution (see the fits in Fig. 13b). As one expects, higher transient T_e is reached at higher excitation density.

Now, using Eq. (19) with the temperature dependence $C_\mathrm{e}(T_\mathrm{e})$ given by Eq. (24) and with the values of $\hbar\omega_\gamma$, $\mathcal{V}$, F, T_env, and T_e corresponding to the experiment-based plots in Fig. 13c, we obtain the possible range of values $3 - 5\,\mathrm{mJ/mol\,K^2}$ for the parameter c entering Eq. (24). In the actual simulations, we use $c = 4\,\mathrm{mJ/mol\,K^2}$.

* p_dolgirev@g.harvard.edu; Present address: Department of Physics, Harvard University, Cambridge, Massachusetts, 02138, USA
† arozhkov@gmail.com
‡ b.fine@skoltech.ru

[1] C. W. Luo, H. P. Lo, C. H. Su, I. H. Wu, Y.-J. Chen, K. H. Wu, J.-Y. Lin, T. M. Uen, J. Y. Juang, and T. Kobayashi, "Doping dependence of the ultrafast electronic dynamics of $Y_{1-x}Pr_xBa_2Cu_3O_{7-\delta}$ thin-film superconductors from femtosecond optical spectroscopy," Phys. Rev. B **82**, 104512 (2010).
[2] E. E. M. Chia, D. Talbayev, J.-X. Zhu, H. Q. Yuan, T. Park, J. D. Thompson, C. Panagopoulos, G. F. Chen, J. L. Luo, N. L. Wang, et al., "Ultrafast Pump-Probe Study of Phase Separation and Competing Orders in the Underdoped $(Ba,\mathbf{K})Fe_2As_2$ Superconductor," Phys. Rev. Lett. **104**, 027003 (2010).
[3] R. Yusupov, T. Mertelj, V. V. Kabanov, S. Brazovskii, P. Kusar, J.-H. Chu, I. R. Fisher, and D. Mihailovic, "Coherent dynamics of macroscopic electronic order through a symmetry breaking transition," Nat. Phys. **6**, 681 (2010).
[4] D. Mihailovic, T. Mertelj, V. V. Kabanov, and S. Brazovskii, "Coherent topological defect dynamics and collective modes in superconductors and electronic crystals," J. Phys.: Condens. Matter **25**, 404206 (2013).
[5] T. Mertelj, P. Kusar, V. V. Kabanov, P. Giraldo-Gallo, I. R. Fisher, and D. Mihailovic, "Incoherent Topological Defect Recombination Dynamics in $TbTe_3$," Phys. Rev. Lett. **110**, 156401 (2013).
[6] C. Zhang, W. Li, B. Gray, B. He, Y. Wang, F. Yang, X. Wang, J. Chakhalian, and M. Xiao, "Ultrafast pump-probe spectroscopic signatures of superconducting and pseudogap phases in $YBa_2Cu_3O_{7-\delta}$ films," J. Appl. Phys. **113**, 083901 (2013).

[7] H. Suzuki, K. Okazaki, T. Yamamoto, T. Someya, M. Okada, K. Koshiishi, M. Fujisawa, T. Kanai, N. Ishii, M. Nakajima, et al., "Ultrafast melting of spin density wave order in $BaFe_2As_2$ observed by time- and angle-resolved photoemission spectroscopy with extreme-ultraviolet higher harmonic generation," Phys. Rev. B **95**, 165112 (2017).

[8] A. Zong, A. Kogar, Y.-Q. Bie, T. Rohwer, C. Lee, E. Baldini, E. Ergecen, M. B. Yilmaz, B. Freelon, E. J. Sie, et al., "Evidence for topological defects in a photoinduced phase transition," Nat. Phys. **15**, 27 (2019).

[9] M. Naseska, A. Pogrebna, G. Cao, Z. A. Xu, D. Mihailovic, and T. Mertelj, "Ultrafast destruction and recovery of the spin density wave order in iron-based pnictides: A multipulse optical study," Phys. Rev. B **98**, 035148 (2018).

[10] F. Schmitt, P. S. Kirchmann, U. Bovensiepen, R. G. Moore, L. Rettig, M. Krenz, J.-H. Chu, N. Ru, L. Perfetti, D. H. Lu, et al., "Transient Electronic Structure and Melting of a Charge Density Wave in $TbTe_3$," Science **321**, 1649 (2008).

[11] M. Eichberger, H. Schäfer, M. Krumova, M. Beyer, J. Demsar, H. Berger, G. Moriena, G. Sciaini, and R. J. D. Miller, "Snapshots of cooperative atomic motions in the optical suppression of charge density waves," Nature **468**, 799 (2010).

[12] S. Hellmann, M. Beye, C. Sohrt, T. Rohwer, F. Sorgenfrei, H. Redlin, M. Kalläne, M. Marczynski-Bühlow, F. Hennies, M. Bauer, et al., "Ultrafast Melting of a Charge-Density Wave in the Mott Insulator $1T-TaS_2$," Phys. Rev. Lett. **105**, 187401 (2010).

[13] T. Rohwer, S. Hellmann, M. Wiesenmayer, C. Sohrt, A. Stange, B. Slomski, A. Carr, Y. Liu, L. M. Avila, M. Kalläne, et al., "Collapse of long-range charge order tracked by time-resolved photoemission at high momenta," Nature **471**, 490 (2011).

[14] J. C. Petersen, S. Kaiser, N. Dean, A. Simoncig, H. Y. Liu, A. L. Cavalieri, C. Cacho, I. C. E. Turcu, E. Springate, F. Frassetto, et al., "Clocking the Melting Transition of Charge and Lattice Order in $1T-TaS_2$ with Ultrafast Extreme-Ultraviolet Angle-Resolved Photoemission Spectroscopy," Phys. Rev. Lett. **107**, 177402 (2011).

[15] N. Erasmus, M. Eichberger, K. Haupt, I. Boshoff, G. Kassier, R. Birmurske, H. Berger, J. Demsar, and H. Schwoerer, "Ultrafast Dynamics of Charge Density Waves in $4H_b-TaSe_2$ Probed by Femtosecond Electron Diffraction," Phys. Rev. Lett. **109**, 167402 (2012).

[16] L. Rettig, R. Cortés, J.-H. Chu, I. R. Fisher, F. Schmitt, R. G. Moore, Z.-X. Shen, P. S. Kirchmann, M. Wolf, and U. Bovensiepen, "Persistent order due to transiently enhanced nesting in an electronically excited charge density wave," Nat. Commun. **7**, 10459 (2016).

[17] R. G. Moore, W. S. Lee, P. S. Kirchman, Y. D. Chuang, A. F. Kemper, M. Trigo, L. Patthey, D. H. Lu, O. Krupin, M. Yi, et al., "Ultrafast resonant soft x-ray diffraction dynamics of the charge density wave in $TbTe_3$," Phys. Rev. B **93**, 024304 (2016).

[18] K. Haupt, M. Eichberger, N. Erasmus, A. Rohwer, J. Demsar, K. Rossnagel, and H. Schwoerer, "Ultrafast Metamorphosis of a Complex Charge-Density Wave," Phys. Rev. Lett. **116**, 016402 (2016).

[19] S. Vogelgesang, G. Storeck, J. G. Horstmann, T. Diekmann, M. Sivis, S. Schramm, K. Rossnagel, S. Schäfer, and C. Ropers, "Phase ordering of charge density waves traced by ultrafast low-energy electron diffraction," Nat. Phys. **14**, 184 (2017).

[20] C. Laulhé, T. Huber, G. Lantz, A. Ferrer, S. O. Mariager, S. Grübel, J. Rittmann, J. A. Johnson, V. Esposito, A. Lübcke, et al., "Ultrafast Formation of a Charge Density Wave State in $1T-TaS_2$: Observation at Nanometer Scales Using Time-Resolved X-Ray Diffraction," Phys. Rev. Lett. **118**, 247401 (2017).

[21] A. Zong, P. E. Dolgirev, A. Kogar, E. Ergeen, M. B. Yilmaz, Y.-Q. Bie, T. Rohwer, I.-C. Tung, J. Straquadine, X. Wang, et al., "Dynamical slowing down in an ultrafast photo-induced phase transition," (2019), arXiv:1902.10109.

[22] M. Trigo, P. Giraldo-Gallo, M. E. Kozina, T. Henighan, M. P. Jiang, H. Liu, J. N. Clark, M. Chollet, J. M. Glownia, D. Zhu, et al., "Coherent order parameter dynamics in $SmTe_3$," Phys. Rev. B **99**, 104111 (2019).

[23] A. Kogar, A. Zong, P. E. Dolgirev, X. Shen, J. Straquadine, Y.-Q. Bie, X. Wang, T. Rohwer, I.-C. Tung, Y. Yang, et al., "Light-induced charge density wave in $LaTe_3$," (2019), arXiv:1904.07472.

[24] F. Zhou, J. Williams, C. D. Malliakas, M. G. Kanatzidis, A. F. Kemper, and C.-Y. Ruan, "Nonequilibrium dynamics of spontaneous symmetry breaking into a hidden state of charge-density wave," (2019), arXiv:1904.07120.

[25] L. P. Gor'kov and G. Grüner, eds., *Charge Density Waves in Solids*, vol. 25 (North-Holland, 1989).

[26] G. Grüner, "The dynamics of charge-density waves," Rev. Mod. Phys. **60**, 1129 (1988).

[27] D. Le Bolloc'h, V. L. R. Jacques, N. Kirova, J. Dumas, S. Ravy, J. Marcus, and F. Livet, "Observation of Correlations Up To the Micrometer Scale in Sliding Charge-Density Waves," Phys. Rev. Lett. **100**, 096403 (2008).

[28] P. Monceau, "Electronic crystals: an experimental overview," Adv. Phys. **61**, 325 (2012).

[29] E. Pinsolle, N. Kirova, V. L. R. Jacques, A. A. Sinchenko, and D. Le Bolloc'h, "Creep, Flow, and Phase Slippage Regimes: An Extensive View of the Sliding Charge-Density Wave Revealed by Coherent X-ray Diffraction," Phys. Rev. Lett. **109**, 256402 (2012).

[30] S. Girault, A. H. Moudden, and J. P. Pouget, "Critical x-ray scattering at the Peierls transition of the blue bronze," Phys. Rev. B **39**, 4430 (1989).

[31] N. Ru, C. L. Condron, G. Y. Margulis, K. Y. Shin, J. Laverock, S. B. Dugdale, M. F. Toney, and I. R. Fisher, "Effect of chemical pressure on the charge density wave transition in rare-earth tritellurides $R\mathrm{Te}_3$," Phys. Rev. B **77**, 035114 (2008).

[32] M. Hoesch, A. Bosak, D. Chernyshov, H. Berger, and M. Krisch, "Giant Kohn Anomaly and the Phase Transition in Charge Density Wave $ZrTe_3$," Phys. Rev. Lett. **102**, 086402 (2009).

[33] L. Stojchevska, I. Vaskivskyi, T. Mertelj, P. Kusar, D. Svetin, S. Brazovskii, and D. Mihailovic, "Ultrafast Switching to a Stable Hidden Quantum State in an Electronic Crystal," Science **344**, 177 (2014).

[34] M. Yoshida, Y. Zhang, J. Ye, R. Suzuki, Y. Imai, S. Kimura, A. Fujiwara, and Y. Iwasa, "Controlling charge-density-wave states in nano-thick crystals of 1T-TaS_2," Sci. Rep. **4**, 7302 (2014).

[35] I. Vaskivskyi, I. A. Mihailovic, S. Brazovskii, J. Gospodaric, T. Mertelj, D. Svetin, P. Sutar, and D. Mihailovic, "Fast electronic resistance switching involving hidden charge density wave states," Nat. Commun. **7**, 11442 (2016).

[36] P. Karpov and S. Brazovskii, "Modeling of networks and globules of charged domain walls observed in pump and pulse induced states," Sci. Rep. **8**, 4043 (2018).

[37] P. Monçeau, N. P. Ong, A. M. Portis, A. Meerschaut, and J. Rouxel, "Electric Field Breakdown of Charge-Density-Wave–Induced Anomalies in $NbSe_3$," Phys. Rev. Lett. **37**, 602 (1976).

[38] B. Riccó, "Fermi surface and charge density waves in niobium diselenide," Solid State Commun. **22**, 331 (1977).

[39] S. Tanda, T. Sambongi, T. Tani, and S. Tanaka, "X-Ray Study of Charge Density Wave Structure in 1T-TaS_2," J. Phys. Soc. Jpn. **53**, 476 (1984).

[40] Pouget, J.P., Kagoshima, S., Schlenker, C., and Marcus, J., "Evidence for a Peierls transition in the blue bronzes $K_{0.30}MoO_3$ and $Rb_{0.30}MoO_3$," J. Physique Lett. **44**, 113 (1983).

[41] E. DiMasi, M. C. Aronson, J. F. Mansfield, B. Foran, and S. Lee, "Chemical pressure and charge-density waves in rare-earth tritellurides," Phys. Rev. B **52**, 14516 (1995).

[42] G.-H. Gweon, J. D. Denlinger, J. A. Clack, J. W. Allen, C. G. Olson, E. DiMasi, M. C. Aronson, B. Foran, and S. Lee, "Direct Observation of Complete Fermi Surface, Imperfect Nesting, and Gap Anisotropy in the High-Temperature Incommensurate Charge-Density-Wave Compound $SmTe_3$," Phys. Rev. Lett. **81**, 886 (1998).

[43] J. Laverock, S. B. Dugdale, Z. Major, M. A. Alam, N. Ru, I. R. Fisher, G. Santi, and E. Bruno, "Fermi surface nesting and charge-density wave formation in rare-earth tritellurides," Phys. Rev. B **71**, 085114 (2005).

[44] N. Ru and I. R. Fisher, "Thermodynamic and transport properties of YTe_3, $LaTe_3$, and $CeTe_3$," Phys. Rev. B **73**, 033101 (2006).

[45] M. Lavagnini, M. Baldini, A. Sacchetti, D. Di Castro, B. Delley, R. Monnier, J.-H. Chu, N. Ru, I. R. Fisher, P. Postorino, et al., "Evidence for coupling between charge density waves and phonons in two-dimensional rare-earth tritellurides," Phys. Rev. B **78**, 201101 (2008).

[46] R. V. Yusupov, T. Mertelj, J.-H. Chu, I. R. Fisher, and D. Mihailovic, "Single-Particle and Collective Mode Couplings Associated with 1- and 2-Directional Electronic Ordering in Metallic $R\mathrm{Te}_3$ (R = Ho, Dy, Tb)," Phys. Rev. Lett. **101**, 246402 (2008).

[47] H.-M. Eiter, M. Lavagnini, R. Hackl, E. A. Nowadnick, A. F. Kemper, T. P. Devereaux, J.-H. Chu, J. G. Analytis, I. R. Fisher, and L. Degiorgi, "Alternative route to charge density wave formation in multiband systems," PNAS **110**, 64 (2013).

[48] D. Le Bolloc'h, A. A. Sinchenko, V. L. R. Jacques, L. Ortega, J. E. Lorenzo, G. A. Chahine, P. Lejay, and P. Monceau, "Effect of dimensionality on sliding charge density waves: The quasi-two-dimensional $TbTe_3$ system probed by coherent x-ray diffraction," Phys. Rev. B **93**, 165124 (2016).

[49] B. F. Hu, B. Cheng, R. H. Yuan, T. Dong, and N. L. Wang, "Coexistence and competition of multiple charge-density-wave orders in rare-earth tritellurides," Phys. Rev. B **90**, 085105 (2014).

[50] A. A. Sinchenko, P. D. Grigoriev, P. Lejay, and P. Monceau, "Linear magnetoresistance in the charge density wave state of quasi-two-dimensional rare-earth tritellurides," Phys. Rev. B **96**, 245129 (2017).

[51] S. Artemenko and A. Volkov, "Contribution to the theory of kinetic phenomena in Peierls dielectics," Sov. Phys. JETP **53**, 1050 (1981).

[52] S. N. Artemenko, "Model of charge-density-wave current conversion and phase-slip dynamics in mesoscopic samples," Phys. Rev. B **67**, 125420 (2003).

[53] Y. Takane, M. Hayashi, and H. Ebisawa, "Time-Dependent GinzburgLandau Equation and Boltzmann Transport Equation for Charge-Density-Wave Conductors," J. Phys. Soc. Jpn. **85**, 084709 (2016).

[54] J. K. Freericks, O. P. Matveev, W. Shen, A. M. Shvaika, and T. P. Devereaux, "Theoretical description of pump/probe experiments in electron-mediated charge-density-wave insulators," Phys. Scr. **92**, 034007 (2017).

[55] W. Shen, Y. Ge, A. Y. Liu, H. R. Krishnamurthy, T. P. Devereaux, and J. K. Freericks, "Nonequilibrium "Melting" of a Charge Density Wave Insulator via an Ultrafast Laser Pulse," Phys. Rev. Lett. **112**, 176404 (2014).

[56] O. P. Matveev, A. M. Shvaika, T. P. Devereaux, and J. K. Freericks, "Time-domain pumping a quantum-critical charge density wave ordered material," Phys. Rev. B **94**, 115167 (2016).

[57] Y. Wang, M. Claassen, C. D. Pemmaraju, C. Jia, B. Moritz, and T. P. Devereaux, "Theoretical understanding of photon spectroscopies in correlated materials in and out of equilibrium," Nature Reviews Materials **3**, 312 (2018).

[58] W. L. McMillan, "Time-dependent Laudau theory of charge-density waves in transition-metal dichalcogenides," Phys. Rev. B **12**, 1197 (1975).

[59] H. Schäfer, V. V. Kabanov, M. Beyer, K. Biljakovic, and J. Demsar, "Disentanglement of the Electronic and Lattice Parts of the Order Parameter in a 1D Charge Density Wave System Probed by Femtosecond Spectroscopy," Phys. Rev. Lett. **105**, 066402 (2010).

[60] H. Schaefer, V. V. Kabanov, and J. Demsar, "Collective modes in quasi-one-dimensional charge-density wave systems probed by femtosecond time-resolved optical studies," Phys. Rev. B **89**, 045106 (2014).

[61] I. K. Schuller and K. E. Gray, "Time-Dependent Ginzburg-Landau: From Single Particle to Collective Behavior," J. Supercond. Novel Magn. **19**, 401 (2006).

[62] P. Beaud, A. Caviezel, S. O. Mariager, L. Rettig, G. Ingold, C. Dornes, S.-W. Huang, J. A. Johnson, M. Radovic, T. Huber, et al., "A time-dependent order parameter for ultrafast photoinduced phase transitions," Nat. Mater. **13**, 923 (2014).

[63] N. Kopnin, *Theory of Nonequilibrium Superconductivity*, vol. 110 of *International Series of Monographs on Physics* (Oxford University Press, 2001).

[64] L. Perfetti, P. A. Loukakos, M. Lisowski, U. Bovensiepen, H. Eisaki, and M. Wolf, "Ultrafast Electron Relaxation in Superconducting $Bi_2Sr_2CaCu_2O_{8+\delta}$ by Time-Resolved Photoelectron Spectroscopy," Phys. Rev. Lett. **99**, 197001 (2007).

[65] B. Mansart, D. Boschetto, A. Savoia, F. Rullier-Albenque, F. Bouquet, E. Papalazarou, A. Forget, D. Colson, A. Rousse, and M. Marsi, "Ultrafast transient response and electron-phonon coupling in the iron-pnictide superconductor $Ba(Fe_{1-x}Co_x)_2As_2$," Phys. Rev. B **82**, 024513 (2010).

[66] Z. Tao, T.-R. T. Han, and C.-Y. Ruan, "Anisotropic electron-phonon coupling investigated by ultrafast electron crystallography: Three-temperature model," Phys. Rev. B **87**, 235124 (2013).

[67] M. Kaganov, E. Lifshitz, and L. Tanatarov, "Relaxation between electrons and the crystalline lattice," Sov. Phys.

JETP **4**, 173 (1957).
[68] S. Anisimov, B. Kapeliovich, and T. Perel'man, "Electron emission from metal surfaces exposed to ultrashort laser pulses," Zh. Eksp. Teor. Fiz **66**, 776 (1974).
[69] J. K. Chen, W. P. Latham, and J. E. Beraun, "The role of electronphonon coupling in ultrafast laser heating," J. Laser Appl. **17**, 63 (2005).
[70] M. Maschek, S. Rosenkranz, R. Heid, A. H. Said, P. Giraldo-Gallo, I. R. Fisher, and F. Weber, "Wave-vector-dependent electron-phonon coupling and the charge-density-wave transition in $TbTe_3$," Phys. Rev. B **91**, 235146 (2015).
[71] M. Maschek, D. A. Zocco, S. Rosenkranz, R. Heid, A. H. Said, A. Alatas, P. Walmsley, I. R. Fisher, and F. Weber, "Competing soft phonon modes at the charge-density-wave transitions in $DyTe_3$," Phys. Rev. B **98**, 094304 (2018).
[72] G. Grüner, *Density Waves In Solids* (Addison-Wesley Publishing Company, 1994).
[73] T. Huber, S. O. Mariager, A. Ferrer, H. Schäfer, J. A. Johnson, S. Grübel, A. Lübcke, L. Huber, T. Kubacka, C. Dornes, et al., "Coherent Structural Dynamics of a Prototypical Charge-Density-Wave-to-Metal Transition," Phys. Rev. Lett. **113**, 026401 (2014).
[74] J.-C. Zheng, Y. Zhu, L. Wu, and J. W. Davenport, "On the sensitivity of electron and X-ray scattering factors to valence charge distributions," J. Appl. Crystallogr. **38**, 648 (2005).
[75] A. W. Overhauser, "Observability of Charge-Density Waves by Neutron Diffraction," Phys. Rev. B **3**, 3173 (1971).
[76] Z. Lin, L. V. Zhigilei, and V. Celli, "Electron-phonon coupling and electron heat capacity of metals under conditions of strong electron-phonon nonequilibrium," Phys. Rev. B **77**, 075133 (2008).
[77] V. Brouet, W. L. Yang, X. J. Zhou, Z. Hussain, N. Ru, K. Y. Shin, I. R. Fisher, and Z. X. Shen, "Fermi Surface Reconstruction in the CDW State of $CeTe_3$ Observed by Photoemission," Phys. Rev. Lett. **93**, 126405 (2004).
[78] J. Demsar and T. Dekorsy, in *Optical Techniques for Solid-State Materials Characterization*, edited by R. Prasankumar and A. Taylor (CRC Press, 2016), pp. 291–328.
[79] Y. H. Wang, D. Hsieh, E. J. Sie, H. Steinberg, D. R. Gardner, Y. S. Lee, P. Jarillo-Herrero, and N. Gedik, "Measurement of Intrinsic Dirac Fermion Cooling on the Surface of the Topological Insulator Bi_2Se_3 Using Time-Resolved and Angle-Resolved Photoemission Spectroscopy," Phys. Rev. Lett. **109**, 127401 (2012).
[80] V. Brouet, W. L. Yang, X. J. Zhou, Z. Hussain, R. G. Moore, R. He, D. H. Lu, Z. X. Shen, J. Laverock, S. B. Dugdale, et al., "Angle-resolved photoemission study of the evolution of band structure and charge density wave properties in $R\mathrm{Te}_3$ (R = Y, La, Ce, Sm, Gd, Tb, and Dy)," Phys. Rev. B **77**, 235104 (2008).
[81] W. S. Fann, R. Storz, H. W. K. Tom, and J. Bokor, "Direct measurement of nonequilibrium electron-energy distributions in subpicosecond laser-heated gold films," Phys. Rev. Lett. **68**, 2834 (1992).
[82] Y. Ishida, T. Togashi, K. Yamamoto, M. Tanaka, T. Taniuchi, T. Kiss, M. Nakajima, T. Suemoto, and S. Shin, "Non-thermal hot electrons ultrafastly generating hot optical phonons in graphite," Sci. Rep. **1**, 64 (2011).